Thesis for the degree of Doctor of Philosophy
in the Natural Sciences

---

# Structural characterization of electron transfer in *D.m* (6-4) photolyase by time-resolved X-ray crystallography

---

Andrea Cellini


UNIVERSITY OF GOTHENBURG

Department of Chemistry and Molecular Biology

Gothenburg, 2022

Thesis for the degree of Doctor of Philosophy
in the Natural Sciences

Structural characterization of electron transfer in *D.m* (6-4) photolyase by time-resolved X-ray crystallography

Andrea Cellini

**Cover:** The difference electron density map at 300 ms after light activation of *Drosophila Melanogaster* (6-4) photolyase.


ISBN 978-91-8069-011-9 (Print)
ISBN 978-91-8069-012-6 (PDF)
Available online at http://hdl.handle.net/2077/73657

Department of Chemistry and Molecular Biology
Division of Biochemistry and Structural Biology
University of Gothenburg
SE-405 30, Göteborg, Sweden
Printed by Stema Specialtryck AB
Borås, Sweden, 2022

Tryckssak
3041 0234

# Abstract

Photolyases are flavoproteins widely spread in bacteria, archea, fungi, plants and animals. These enzymes absorb blue light and use it as an energy source for repairing damages that are induced on DNA after a prolonged exposure to UV-light. The mechanism of DNA repair in photolyases requires a first step of photo-excitation known as photoactivation. During this process, the chromophore uptakes an electron from a close tryptophan. This event triggers an electron transfer along a chain of tryptophans and results into the reduction of the chromophore to its catalytic form.

This thesis is focusing on unravelling the structural changes associated with photoactivation in a photolyase from *Drosophila Melanogaster*. We employed time-resolved serial crystallography as the main technique of investigation. In the three papers, we present the crystallography techniques and conditions that were used for time-resolved experiments in synchrotron and in x-ray free electron laser facilities (XFEL). At first, we solved the structure of the protein in its resting state and then we characterized the structural changes that occur after light activation. We recorded data at different time delays from illumination ranging from ps to ms. The findings show structural changes around the chromophore and the tryptophans involved in the electron transfer.

These results contribute to the understanding of the structural adaptation of photolyase during the first electron transfer process. However, further studies are needed to structurally characterized the second step of photoactivation and the process of DNA-repair.

# Publications

This thesis consists of the following research papers:

**PAPER I:** **Andrea Cellini***, Weixiao Yuan Wahlgren*, Léocadie Henry, Suraj Pandey, Swagatha Ghosh, Leticia Castillon, Elin Claesson, Heikki Takala, Joachim Kübel, Amke Nimmrich, Valentina Kuznetsova, Eriko Nango, So Iwata, So Owada, Emina A. Stojković, Marius Schmidt, Janne A. Ihalainen and Sebastian Westenhoff. "The three-dimensional structure of Drosophila melanogaster (6–4) photolyase at room temperature". Acta Crystallographica Section D: Structural Biology, 2021, 77.8: 1001-1009. * Equally contributed.

**PAPER II:** **Andrea Cellini**, Weixiao Yuan Wahlgren, Madan Kumar, Amke Nimmrich, Tek Malla, Antonia Furrer, Melissa Carrillo, Jennifer Mutisya, Emma V. Beale , Florian Dworkowskic, Camilla Bacellar , Joerg Standfuss, Tobias Weinert, Janne A. Ihalainen and Sebastian Westenhoff. "Ultrafast conformational changes of the photoactivation of a (6-4) photolyase captured by time-resolved crystallography" (Manuscript).

**PAPER III:** **Andrea Cellini**, Madan Kumar Shankar, Weixiao Yuan Wahlgren, Amke Nimmrich, Antonia Furrer, Daniel James, Maximilian Wranik, Sylvain Aumonier, Emma V. Beale, Florian Dworkowski, Joerg Standfuss, Tobias Weinert and Sebastian Westenhoff. "Structural basis of the radical pair state in photolyases and cryptochromes". Chemical Communications, 2022, 58.31: 4889-4892.

Papers that I have co-authored but that are not included in this thesis and are not related to photolyase:

**PAPER IV:** Elin Claesson, Weixiao Yuan Wahlgren, Heikki Takala, Suraj Pandey, Leticia Castillon, Valentyna Kuznetsova, Léocadie Henry, Matthijs Panman, Melissa Carrillo, Joachim Kübel, Rahul Nanekar, Linnéa Isaksson, Amke Nimmrich, **Andrea Cellini**, Dmitry Morozov, Michał Maj, Moona Kurttila, Robert Bosman, Eriko Nango, Rie Tanaka, Tomoyuki Tanaka, Luo Fangjia, So Iwata, Shigeki Owada, Keith Moffat, Gerrit Groenhof, Emina A Stojković, Janne A Ihalainen, Marius Schmidt and Sebastian Westenhoff. "The primary structural photoresponse of phytochrome proteins captured by a femtosecond X-ray laser". Elife, 2020, 9: e53514.

**PAPER V:** Léocadie Henry, Oskar Berntsson, Matthijs Panman, **Andrea Cellini**, Ashley Hughes, Irena Kosheleva, Robert Henning and Sebastian Westenhoff. "New light on the mechanism of phototransduction in phototropin". Biochemistry, 2020, 59.35: 3206-3215.

# Contribution report

**PAPER I:** I purified the protein, screened buffers and additives for macrocrystallization of the protein. I optimized the batch conditions for microcrystallization. I analyzed data and refined the structure x-ray diffraction data. For the room temperature data, I refined the structure. I co-wrote the paper and made figures for the paper.

**PAPER II:** I prepared the protein and the crystals. I analyzed the x-ray data and refined the dark and light structures. I made the figures and co-wrote the manuscript.

**PAPER III:** I purified the protein and crystallized it. I performed data analysis on the fly together with other colleagues. I refined the light structure and co-refined the dark structure, made the figures for the paper and co-wrote the paper.

# Abbreviations

Here follows a list of the different abbreviations used in this thesis.

| | |
|---|---|
| **A.nidulans** | **A**nacystis nidulans |
| **CC** | **C**orrelation **C**oefficient |
| **CPD** | **C**yclobutane **P**yrimidine **D**imer |
| **CPF** | **C**ryptochrome and **P**hotolyase **F**amily |
| **CCE** | **C**ryptochrome **C**-terminal **E**xtension |
| **DLZ** | 6,7-**D**dimethyl-8-ribity**L**luma**Z**ine |
| **D.m** | **D**rosophila **M**elanogaster |
| **E.coli** | **E**scherichia **C**oli |
| **FAD** | **F**lavin **A**denine **D**inucleotide |
| **FMN** | **F**lavin **M**ono**N**ucleotide |
| **GDVN** | **G**as **D**ynamic **V**irtual **N**ozzle |
| **HEC** | **H**ydroxy**E**thyl-**C**ellulose |
| **IPTG** | **I**so**P**ropyl $\beta$- d-1-**T**hio**G**alactopyranoside |
| **LCP** | **L**ipid **C**ubic **P**hase |
| **MTHF** | **M**ethenyl**T**etra**h**ydro**F**olate |
| **MX** | **M**acrocrystallography |
| **PDB** | **P**rotein **D**ata **B**ank |
| **PEG** | **P**oly**E**thylene **G**lycol |
| **PHR** | **P**hotolyase **H**omology **R**egion |
| **PL** | **P**hoto**L**yase |
| **SACLA** | **S**pring-8 **A**ngstrom **C**ompact free electron **LA**ser |
| **SEC** | **S**ize **E**sclusion **C**hromatography |
| **SFX** | **S**erial **F**emtosecond crystallography |
| **SLS** | **S**wiss **L**ight **S**ource |
| **SSX** | **S**erial **S**ynchrotron crystallography |
| **XFEL** | **X**-ray **F**ree-**E**lectron **L**aser |
| **X.laevis** | **X**enopus **L**aevis |

# Contents

# Chapter 1

# Introduction

In Chapter 1, I report a summary of cryptochrome and photolyase family (CPF) with a focus on photolyases. Here, I am presenting the classification, structure, and function of photolyases.

## 1.1 UV damages of DNA

Sunlight governs many aspects of plants and animal physiology. In plants light controls processes such as seed development, de-etiolation [1] and flowering [2]. In animals, it is important for vision, thermoregulation and activation of vitamin D [3]. Nevertheless, the ultraviolet (UV) content in sunlight can be deleterious and its negative effect is intensifying with the reduction of the UV-filtering ozone layer [4].

UV-light is an electromagnetic radiation with wavelength from 100 to 400 nm. Macromolecules such as proteins and polinucleotides can absorb UV-light and are susceptible to UV-dependent photo-oxidation which results in a genotoxic and cytotoxic effects in living organisms. [5, 6].

In DNA, UV-B and UV-C light induces different types of damages or lesions: either a breakage of the DNA strand or the formation of covalent bonds between adjacent pyrimidines such as cyclobutane pyrimidine dimer (CPD) and (6-4) pyrimidine-pyrimidone photoproduct (6-4 PP) (Fig.1.1). Among the possible UV-induced lesions, CPDs are the major photo-adducts accounting for 75% of the UV-induced DNA lesions [7, 8]. The remnant 25 % is represented by 6-4 PPs. 6-4 PPs are generated after isomerization of an oxetane/azetidine intermediate and can be converted into their Dewar valence isomer forms by exposure with 320nm UV-B

light [9, 10]. Both CPD and 6-4 PP twist the DNA helix by introducing a kink of 9° and 44° respectively [11]. Therefore, CPD and 6-4 PPs can interfere with DNA replication and transcription [12, 13]. Although 6-4 PPs are the least abundant lesions, they are more mutagenic than CPDs [14].

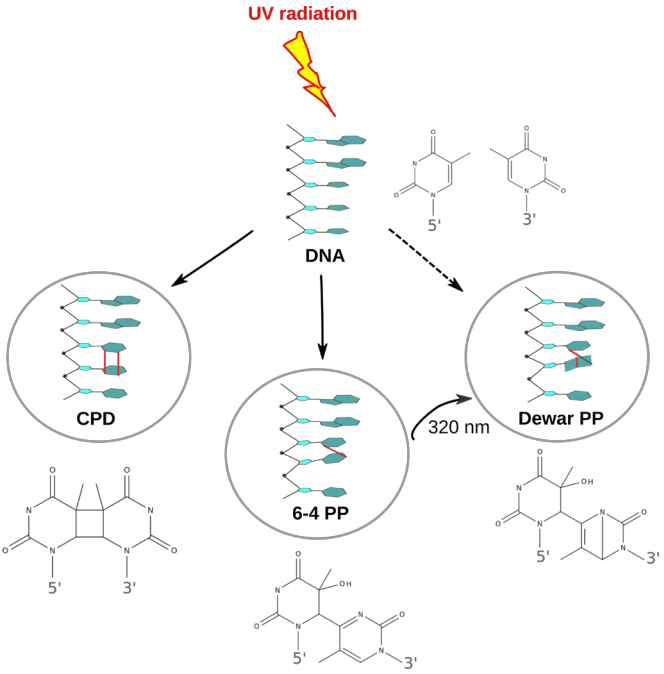


**Figure 1.1:** Schematic representation of CPD and 6-4 PP lesions in DNA. The structures of the CPD thymine-tymine, the (6-4)thymine thymine photoadduct and its Dewar isomer are reported. The structures were adapted from [15].

### 1.1.1 Repair of CPD and 6-4 PP lesions

Throughout evolution, organisms have developed different strategies to fix the CPD and 6-4 PP damages and preserve genome integrity. These strategies can be: photoreduction [16], nucleotide excision repair (NER) and DNA mismatch repair (MMR) [17].

The DNA repair by photoreduction is a light-dependent reversal of either a CPD or a 6-4 PP lesion by enzymes known as photolyases (Fig.

1.2). The function of photolyases is not exclusively dependent on light and they can also exhibit a "dark" activity. In absence of light, photolyase recruits NER proteins into the damaged site that is then restored in a NER-dependent way [18, 19]. NER and MMR mechanisms require the assembling of many proteins that participate in the DNA lesion recognition and ATP-dependent repair. So DNA repair by photoreduction seems to be much more effective and efficient.

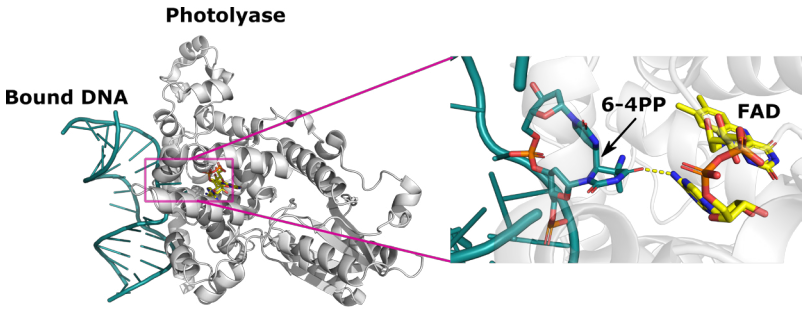


**Figure 1.2:** *D.m*(6-4)PL and its interaction with a (6-4)TC (thymine-cytosine) lesion in a dsDNA (PDB ID: 2WB2).

Here is a short introduction of NER and MMR mechanisms. NER proteins can detect both CPD and 6-4 PPs in a double stranded DNA (dsDNA) and repair them in four steps. At first, an helicase opens the dsDNA at the lesion site, then a nuclease cuts the DNA at the lesion 3' and 5'. Afterwards, a DNA polimerase re-synthesises the DNA that is then ligated by a DNA ligase [20] (Fig. 1.3).

The process of DNA lesion recognition is not always successful. Sometimes, the lesions are overlooked and bypassed during DNA replication by the intervention of DNA polymerase IV and V in *E.coli* and Pol $\eta$ and $\zeta$ in eukaryotes. However, this so-called translesion DNA synthesis is error-prone and increases the chances of mutagenesis by introducing an incorrect nucleotide at the lesion site [21–23]. The resulting mismatch can be resolved via activation of MMR during DNA-replication. In *E.coli*, the mismatch correction begins with a cleavage in the proximity of the lesion, followed by the unwinding of the DNA towards the lesion and the stabilization of the single stranded DNA (ssDNA). Exonucleases cleave

the ssDNA moving from the nicked site towards the DNA damage and the DNA strand is then re-synthesised and ligated [17] (Fig. 1.3).

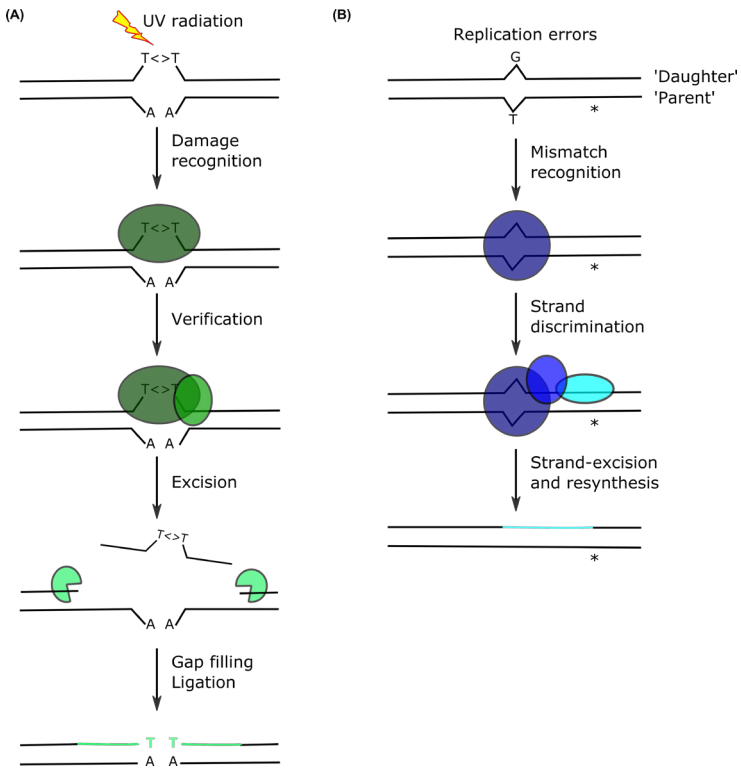


**Figure 1.3:** Basic action mechanism of nucleotide excision repair (NER) and DNA mismatch repair (MMR) in cartoon.

## 1.2 Photolyase/cryptochrome family

Photolyases (PL) are flavoproteins belonging to the Photolyase and Cryptochrome family (CPF). Generally, PLs are classified according to their ability to repair either CPD lesions or (6-4) PP lesions. PLs that repair CPD lesions are called CPD photolyases (CPD-PL), whereas PLs that repair (6-4) PP lesions are called (6-4)pyrimidine-pyrimidone photolyases ((6-4)PL).

CPD-PLs can be further subdivided in three different classes according to their homology in the sequences: class I (mainly in microorganisms), class II (mainly in eukaryotes), class III (related to plant cryptochrome) [24]. Despite the conserved protein structure and function within the three classes, their sequences widely differ and are only 20% identical [25].

(6-4)PLs have been isolated both in eukaryotes and prokaryotes. In some instances, they are co-expressed with CPD-PLs (in *A. thaliana*, *D. melanogaster*, *X. laevis* [26] and *X. maculatus* and *X. couchianus* [27]) whereas in *B. subtilis* and *H. influenzae* neither of them is present [28].

CPF includes also cryptochromes (CRY). Animal cryptochromes are closely related to (6-4)PL as suggested by their sequence homology (40-60%) [25]. They can be further divided in type I (insect CRY), type II (mammals CRY) and type IV (birds, amphibians, reptiles CRY). Type I and II CRYs are regulators of the circadian clock in a light-dependent and light-independent fashion respectively, whereas type IV CRYs are still not well characterized [29]. Plant cryptochromes are closely related to CPD-I. They are purely photoreceptors and they partake in the circadian clock like their animal counterparts [30].

Recently a new subclade of PLs has been identified and named CRY-DASH (Cryptochrome-Drosophila, Arabidopsis, Synechocystis, Human) [31]. The CRY-DASH members are classified as photolyases that can photo-revert a CPD or a 6-4PP lesion in ssDNA [32, 33]. However, in the past years new studies revealed that some CRY-DASH members act as blue light photoreceptors. [34, 35]. For these reasons, the CRY-DASH subclade can be considered the evolutionary link between photolyases and cryptochromes [34].

This classification of CPF proteins according to their functions (Fig. 1.4 ) is rather limiting. Indeed, some CPF proteins can repair both type of lesions, others are able to both repair DNA and regulate the transcription of genes [36, 37].

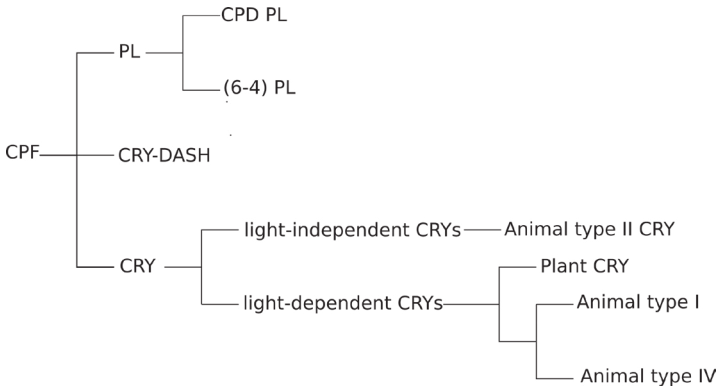


**Figure 1.4:** Functional classification of the CPF protein family.

### 1.2.1 Structural organization of CPF proteins

The CPF proteins share a conserved region called PHR or photolyase homology region. The PHR consists of a N-terminal $\alpha/\beta$ domain and a C-terminal $\alpha$ domain that are interconnecting to each other through a loop (Fig. 1.5). Furthermore, in animal and plant cryptochromes PHRs are extended at the C-terminal with a highly variable tail ranging from 30 to 300 residues [38]. The tail interaction with the PHR controls cryptochromes subcellular localization and maintains them in an auto-inhibited form [39].

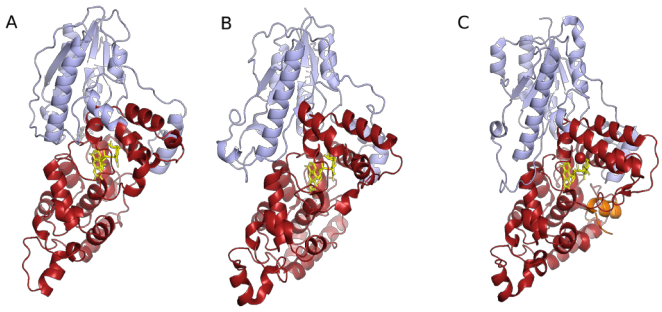


**Figure 1.5:** Examples of CPF members. In A, *E.coli*CPD (PDB:1DPN) [40], in B *A.thalian*(6-4)PL (PDB ID:3FY4) [41], in C, *D.m*CRY (PDB ID: 4GU5) [42] are displayed. The $\alpha/\beta$ domain and the C-terminal $\alpha$ domain are represented in blue and red respectively. The CCE (cryptochrome C-terminal extension) in *D.m*CRY is in orange. FAD are shown in yellow.

The $\alpha$ domain harbours the catalytic chromophore, Flavin adenine dinucleotide (FAD), in a conserved binding pocket. The FAD, as well as the antenna cofactor in the $\alpha/\beta$ domain, is non-covalently bound to the protein and is retained in its binding pocket by a series of hydrogen bonds and hydrophobic interactions (Fig. 1.6). In the PLs proteins, FAD bends in a U-shaped conformation allowing its isoalloxazine group to be in proximity to its adenine moiety. This specific geometry of the chromophore eases the DNA repair as the reduction of the lesion occurs via electron transfer through the adenine [43]. In both CPD-PLs and (6-4)PLs, the adenine moiety of the FAD is in direct contact with the substrate and in (6-4)PLs it also establishes a hydrogen with the conserved H365 that is involved in the repair of DNA [44]. The substrate binding is not only mediated by the FAD but also by the residues around the binding pocket of the FAD and the residues defining the DNA entry access to the catalytic site [45].

There are other conserved features that can be found in the $\alpha$ domain and are connected with the photoactivation process (or reduction of the chromophore) that occurs in PLs: the asparagine near the FAD N5 (N378 in *E.coli*; N386 in *A. nidulans*; N403 in *Dm(6-4)*PLs), a salt bridge between an asparagine and an aspartate underneath the FAD isoalloxazine ring (R368-D397 in *D.m*(6-4)PL and R344-D372 in *E.coli* CPD-PL) [46]

and a conserved triad/tetrad of tryptophan-chain that extends from the protein core to the protein surface.

The $\alpha/\beta$ domain adopts a Rossmann-like fold with five $\beta$ sheets and five $\alpha$ helices which can harbour an antenna chromophore. Five different antenna cofactors have been identified: 5,10-methenyltetrahydrofolte (MTHF) [34, 47, 48], FAD [49], 8-hydroxydeazaflavin (8-HDF) [50–53], Flavin mononucleotide (FMN) [54] and 6,7-dimethyl-8-ribityllumazine (DLZ) [55].

In MTHF-containing photolyases, the MTHF cofactor is allocated in the cleft between N-terminal $\alpha/\beta$ domain and the C-terminal $\alpha$ domain, whereas the other antenna cofactors are found buried in the C-terminal $\alpha$ domain. Structural comparison between the apoenzyme and holoenzyme of 8-HDF photolyases suggests that small rearrangements of a nearby loop (the antenna loop) are important to assure the retention of 8-HDF within the binding site [51, 52].

These antenna cofactors do not take part in the catalytic reaction but upon light activation, the antenna cofactor transfers energy to the FAD in the $\alpha$ domain and increases 10-100 times the rate of DNA repair [26]. The efficiency of energy transfer depends on the distance and orientation between the antenna chromophore and the FAD and varies among photolyases. For instance, it is around 70 % in *E.coli* CPD-PL and 100 % in *A.nidulans* CPD-PL [26].

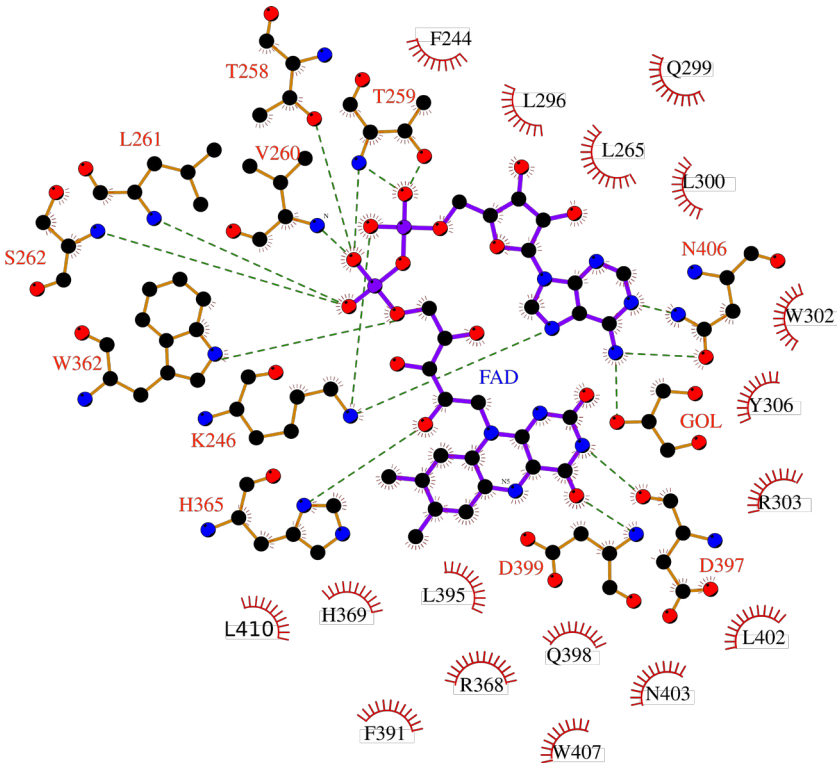


**Figure 1.6:** FAD and its interaction with the surrounding residues in *D.m*(6-4)PL. The image was produced with PDBsum and entry 7AYV **(Paper I)**. Hydrogen bonds are represented by dashed lines and hydrophobic contacts are represented by arches.

### 1.2.2 FAD photoactivation and DNA lesion photoreduction

The light response of CPF proteins can be divided into two steps. The first is common between cryptochromes and PLs and consists of the reduction of the flavin chromophore (photoactivation). The second step differs between them. In PLs, it consists of the repair of DNA lesions (photoreductions), whereas in cryptochromes it consists in the regulation of the circadian clock (not discussed in this thesis) [56].

### FAD Photoactivation

The photoactivation reaction implies a light-triggered electron transfer towards the main chromophore (FAD) and subsequent formation of radical intermediates. The generation of the FAD in a specific redox state is a prerequisite for CPF members in order to repair DNA or activate a signalling cascade. The final and active state at which the FAD can complete its function could be either the fully reduced state ($FADH^-$) or semireduced state ($FAD^-$) depending on the CPF members under examination [26,57].

Generally speaking, FAD can be found in different redox states: fully oxidized (FADox), semireduced ($FAD^-$ or $FADH^{\cdot}$) or fully reduced ($FADH^-$ or $FADH_2$). Each state possesses distinctive spectroscopic characteristics: FADox has 3 peaks in the blue region, $FAD^-$ has higher absorption in near UV region, $FADH^{\cdot}$ can be identified due to its absorbance between 500-650 nm and the fully reduced doesn't absorb in the visible light region [24].

The study of the electron transfer is a complex and challenging task. In PLs, the first electron transfer pathway was identified in *E.coli* CPD-PL and it involves a triad of conserved tryptophans that is extended to a tetrad in animal (6-4)PLs and animal cryptochromes [58,59]. However, during the past years, different electron transfer pathways involving intrinsic electron donors have been reported in many CPF proteins [48,60–64].

The photoactivation process has been studied with time-resolved spectroscopy and up to date, *E.coli* CPD-PL photoactivation has been characterized the most. In *E.coli* CPD-PL (Fig. 1.8), one electron pathway involves a tryptophans triad: W382 ($W_1$), W359 ($W_2$) and W306 ($W_3$). This chain of tryptophans extends from the FAD's pocket towards the surface. Upon light exposure, the FAD is excited by light and extracts one electron from the nearby W382 thus generating the first radical pair $FAD^{\cdot -}$-$W_1H^{\cdot +}$ in 0.4-0.8ps. The electron transfer proceeds along the chain and leads to the formation of the $FAD^{\cdot -}$-$W_2H^{\cdot +}$ in 70 ps and finally the $FAD^{\cdot -}$-$W_3H^{\cdot +}$ in 150ps. Afterwards, $FAD^{\cdot -}$ gets protonated to $FADH^{\cdot}$ and $W_3H^{\cdot +}$ releases a proton to the solvent and later gets reduced by an external reductant. The reaction continues with the photoexcitation of $FADH^{\cdot}$. This generates the $FADH^-$-$W_1H^{\cdot +}$ radical pair in 30 ps followed

by $FADH^{-}$-$W_2H^{\cdot+}$ in less than 4ps. In about 200 ps, the $FADH^{-}$-$W_3H^{\cdot+}$ is stabilized by deprotonation of $W_3H^{\cdot+}$ [65–67].

In (6-4)PLs, a recent transient absorption spectroscopy study on *X.laevis*(6-4)PL reveals that the $FAD^{\cdot-}$-$W_3H^{\cdot+}$ pair forms in less than 20 ns, whereas the $FAD^{\cdot-}$-$W_4H^{\cdot+}$ pair generates in 2.5 $\mu$s. Afterwards the $FAD^{\cdot-}$ gets protonated to $FADH^{\cdot}$ in 200 ms and $W_4H^{\cdot+}$ gets reduced back to $W_4$ [58](Fig. 1.7).

The final FAD redox state seems to be highly dependent on the chemical nature of the residue facing the FAD-N5 atom. In many CPD-I and -II PLs, (6-4)PL and CRY-DASH, the proximal residue to the FAD is an asparagine. In *D.m*-like cryptochromes, this residue is a cysteine whereas in plant cryptochrome it is an aspartate. In the majority of the PLs, the asparagine stabilizes the $FADH^{\cdot}$ by orienting its carbonyl group towards the protonated N5 [68]. In plant cryptochrome, the FAD can be reduced both to $FADH^{\cdot}$ and $FADH^{-}$ as in the previous case but the aspartate can act as a proton shuttle [69]. In insect-like cryptocromes, the presence of a cysteine hinders the formation of $FADH^{\cdot}$ and $FADH^{-}$, favouring the stabilization of the FAD in the anionic radical state, $FAD^{-}$ [70].

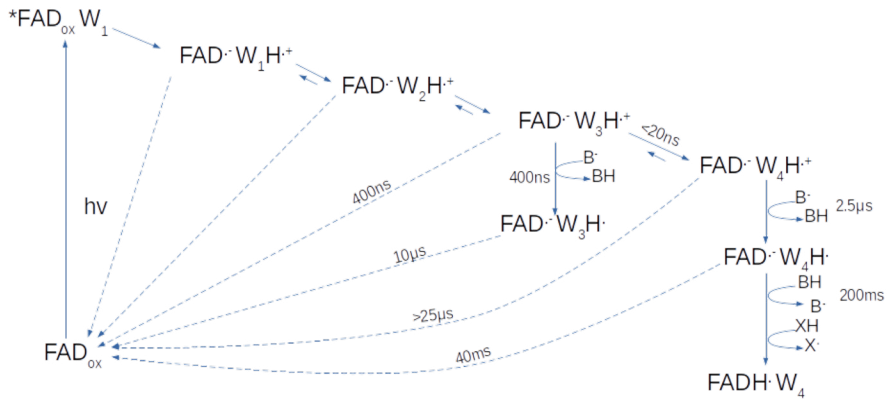


**Figure 1.7:** Photoactivation scheme of $FAD_{ox}$ in *X.laevis*(6-4)PL [58].

### DNA lesions photoreduction

For the photorepair of CPD and 6-4 PPs to happen, firstly the lesion needs to be recognized and bound in a light independent way. Secondly, the photoexcited $FADH^-$ needs to funnel an electron into the lesion (Fig. 1.8) [26, 71].

The repair mechanism for CPD-PLs has been extensively studied and elucidated, whereas it is still a matter of research for (6-4)PLs.

In CPD-PL, the excited $FADH^-$ donates an electron to the CPD lesion through the adenine moiety in 250 ps and in 90 ps the dimer splits into its original pyrimidine-pyrimidine conformation. Afterwards, $FADH^-$ is regenerated by back electron transfer from the lesion and the DNA is released from the catalytic site. The entire process is highly efficient reaching a quantum yield of 0.8-0.9 [72, 73].

For (6-4)PL, the repair mechanism is more complex and requires not only a breakage of a covalent bond like in CPD-PLs but also a transfer of either a -OH or $-NH_2$ group. Although many mechanisms have been proposed [71], the most recent one suggests a two photon mechanism with the formation of an unknown intermediate. According to the latter, the electron transfer to the lesion occurs in 225 ps, an intermediate forms in around 40$\mu$s and the complete restoration of the pyrimidines happens in around 200 ns [74].

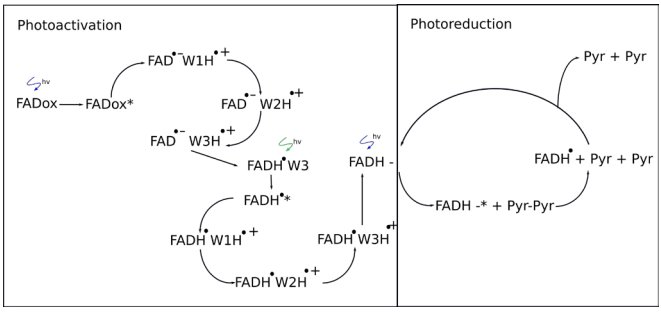


**Figure 1.8:** Simplified scheme of the photoactivation and photoreduction mechanism in a CPD-PL. In the left panel, the photoexcitation of $FAD_{ox}$ results in the formation of several radical pairs involving $FAD^{\cdot -}$ and radical tryptophanyls (W1, W2, W3). Once the last radical pair $FAD^{-}$-$W3H^{\cdot +}$ forms, $FAD^{\cdot -}$ gets protonated to $FADH^{\cdot}$. The process continues with the formation of radical pairs involving $FADH^{\cdot}$ and the conserved tryptophans until full reduction of $FADH^{\cdot}$ to $FADH^{-}$. After the generation of $FADH^{-}$, the photoreduction occurs. This process includes the splitting of the pyrimidine-pyrimidine (Pyr-Pyr)dimer and the transient generation of $FADH^{\cdot}$ which returned to $FADH^{-}$ by back electron transfer from the lesion. After the repair, the DNA is released from the catalytic site.

## 1.3 Scope of the thesis

The structure of *D.m*(6-4)photolyase in its resting state was already published in 2008 [75]. However, the light-induced intermediate states were not structurally characterized. The aim of the thesis is to study these structural rearrangements upon photo-excitation by serial femtosecond x-ray crystallography (SFX) and serial synchrotron crystallography (SSX).

The thesis is structured in four chapters:

**Chapter I: Introduction**. An introduction to the cryptochrome and photolyase family.

**Chapter II: Sample preparation for x-ray crystallography**. A summary of the biochemical methods used in the thesis.

**Chapter III: X-ray diffraction, SFX and SSX**. A description of the main methods to analyze and interpret the data.

**Chapter IV: The early and late events in *D.m*(6-4)photolyase photoresponse**. I summarized the main findings that were discussed in

the manuscripts.

The thesis is based on three papers:

**Paper I (published)**. We reported optimized crystallization conditions for both macrocrystals and microcrystals of *D.m*(6-4)photolyase. We proved that microcrystal can be used for time-resolved serial x-ray crystallography (SX) experiments.

**Paper II (manuscript)**. We described the local structural rearrangement in the first ps of photoactivation in *D.m*(6-4)photolyase.

**Paper III (published)**. We investigated the late events in the photoactivation process and described how these observed structural changes could stabilize the charge separation that occurs during the photoactivation reaction in *D.m*photolyase.

# Chapter 2

# Sample preparation for x-ray crystallography

This thesis is focused on structural studies of *D.m*(6-4) PL by using serial x-ray crystallography. In Chapter 2, I will list and shortly describe what techniques have been employed to express, purify and finally crystallize the protein in order to perform such studies.

## 2.1 Protein expression

Generally, the protein of interest can be isolated by either its native source or by expression of a recombinant DNA in a suitable host. In this project, we used three different vectors for the expression of *D.m*(6-4) photolyase in *E.coli*.

The first plasmid (construct 1) was a gift from Munich University. The gene encoding for a truncated version of the protein was amplified from a cDNA library. It was cloned first in a pDONR201 and then into pDEST007 plasmid through a two step-Gateway reaction in a way that Strep-Tag II was in the N-terminal of the protein [75]. We transformed *Rosetta(DE3)pLysS* cells with the plasmid, grew them at 37 °C in a modified TB supplemented with 100 $\mu$g/mL carbenicillin and 34 $\mu$g/mL chloramphenicol until O.D was in the range 1-1.2 and then induced with 200 ng/mL anhydrotetracycline (ATC) at 16°C. After lysing the cells with Emulsiflex-C3, the debris was spun down and the supernatant was loaded first in a StrepTrapHP column, then HiTrap Heparin HP column and finally into a size exclusion (SEC) column [75]. Every step was performed

in a cold room and under red safe light. The protein yield was significantly low and around 0.07 mg/Litre of culture. We proceeded with performing an expression test, varying the temperature of induction, O.D (optical density) of induction and concentration of antibiotics. From the western blot results, the best condition was achieved by reducing the antibiotics concentration in half and inducing at O.D 1 at 18 °C. Through these minor changes, we could achieve a yield of around 0.3 mg/Litre of culture. These conditions were used in **Paper I**.

The protein yield was still a limiting factor for the upscale production of crystals so we designed and ordered two new constructs with a codon optimized gene. They are both pET21d+ plasmids where the His-tag was cut off by introducing a stop codon. In one case (construct 2)(Fig. 2.1), a Strep-TagII was introduced and in the other no tag was inserted (construct 3). Both plasmids were transformed in *E.coli BL21(DE3)*. The purification was done in a similar way as described above with the exclusion of the StrepTrapHP affinity column step for construct 3. Expression tests were carried out using different media, concentration of Isopropyl $\beta$ d-1-thiogalactopyranoside (IPTG), different O.D and temperature of induction. Construct 3 provided us with higher amount of protein compared with construct 2 and 1. The cells were grown in a Studier-like medium with 50 $\mu$g/mL carbenicillin for 2-3h at 37 °C and moved to 20 °C for 10-12 hours. The final protein yield from construct 3 was 3mg/Litre of culture.

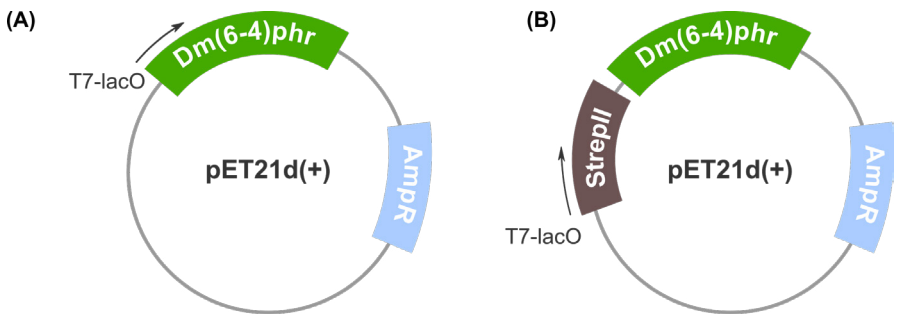


**Figure 2.1:** Construct 2 (A) and construct 3 (B) structure.

## 2.2 Crystallization

X-ray crystallography has been an extremely useful tool for determining the 3-D structure of small molecules or in our case macromolecules. One of the prerequisites for x-ray crystallography is the availability of homogeneous and highly diffracting crystals.

Protein crystals are assemblies of ordered macromolecules held together by non-covalent interactions [76]. Within the crystals, we can identify *unit cells* which correspond to the combination of the crystal lattice and motifs (e.g atoms, molecules etc.). The unit cells can be seen as the crystals building blocks and their translation generates the crystals *per se*. The unit cells and their content can be described by a *space group* which provides information about the crystal symmetry [77].

The process through which we can obtain these ordered assemblies is known as crystallization and can be divided into two phases: nuclei formation and crystal growth. The mentioned processes are both dependent on supersaturation, a non-equilibrium condition that can be reached when the protein is exceeding its solubility limit [78]. Different protein and precipitating agents concentrations determine different levels of supersaturation that are described in the crystallization phase diagram (Fig. 2.2). The diagram can be split into four regions. At high concentration of protein and precipitant, we reached a high level of supersaturation which leads to protein precipitation. At medium level of supersaturation, nucleation occurs. Underneath this zone, we find the metastable area which corresponds to the optimal conditions for the crystals to grow. Below the metastable region, there is the undersaturated region where no crystals can be attained.

There are mainly four methods that are employed for crystallization and all of them can be altered to achieve the supersaturation. The four main methods are: dialysis, microbatch, vapor diffusion and free interface diffusion. The method that I've employed in **Paper I**, **Paper II** and **Paper III** is the vapour diffusion method. In this method, a drop of protein is mixed with precipitating agents and is sitting on or hanging from a support. In this setup, the drop is sitting/hanging on top of a well that contains reservoir at higher concentration of precipitant. Over time, water

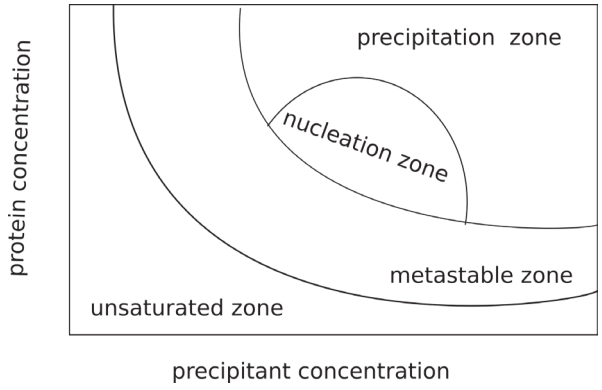


**Figure 2.2:** Crystallization phase diagram.

vapour leaves the drop and moves towards the reservoir until an equilibrium is reached. This controlled dehydration will increase the protein and crystallization reagents concentrations within the drop and supersaturation can be achieved [79].

## 2.3 Microcrystallization

Traditional single x-ray crystallography (MX) requires the acquisition of data from a single large crystal. However, there can be cases where crystals grow only as microcrystals [80] or the methods of choice (i.e. SX and SFX) require smaller sized sample [81]. Besides these factors, the employment of microcrystals has been advantageous for their intrinsic qualities such as lower mosaicity and great robustness. The low mosaicity derives from the lower number of units constituting the crystal and it has been shown to increase data quality [82]. The robustness makes the crystals less prone to any deleterious effects derived from perturbations such as cryocooling, ligands soaking or light illumination for pump-probe studies. Microcrystals are more robust because their smaller dimensions allow perturbations to occur rapidly and uniformly without drastic changes on the crystals' lattice.

Microcrystals can be achieved from macrocrystals as a starting material. There are mainly two approaches to achieve this goal.

One can simply crush the macrocrystal by several means such as vortexing, but the downside of this approach consists of a heterogeneous sample [83]. The problem can be overcome by filtering the crystals albeit the sample loss can become a limiting factor for the success of the experiment. Another issue related to the physical crushing of the crystals is the increase in the crystals' mosaicity and hence the broadening of the *Bragg*'s peaks [84].

In alternative to the latter method, one can opt for batch method crystallization or free interface diffusion.

In the batch method, it is pivotal to have a knowledge of the crystallization diagram in respect to the protein of interest. This method consists of mixing the protein and precipitating agents in a concentration that allows us to reach the nucleation zone immediately. Although the conditions are suitable for nuclei to form, additional seeding (i.e addition of small fragments of crystals) can be performed. The introduction of seeds would increase the nucleation rate and the yield of microcrystals [85] .

In the free interface diffusion technique, the protein solution is placed on top of the mother liquor. Microcrystals will form on the interface between the solutions whereas bigger crystals will form underneath [86].

## 2.4 *D.m*(6-4)PL macro- and micro- crystals

At the beginning of this project, the crystallization methods were oriented towards a more systematic approach. The vector for protein expression (construct 1) was a gift and the crystallization conditions were already determined (20-25% PEG1500, 0.1 M MIB buffer, pH 8.6). However, the original reservoir composition and its variants (in protein concentration, precipitant concentration and pH) were unsuccessful and no crystal could be observed. We switched to a shotgun approach and tested several buffer conditions using commercially available kits. Many hits were found and the highest diffracting conditions (the crystals diffracted at 2.2 Å) were: 0.2 M lithium sulfate monohydrate, 0.1 M bis-tris , pH=6.5 and 25% PEG 3350. The crystals were grown on hanging drop plates at 20 °C. After finding the optimal buffer, we performed a screen of 96 additives. Only two of them provided highly diffracting crystals: 1-butanol (1.9 Å)

and polypropylene glycol P400 (1.79 Å). The next goal was to achieve microcrystals and we opted for two lines of action: sitting drops with seeding at 4 °C and a batch method that was carried out both at 4°C and at 20 °C. The crystal batch was obtained with the following components: 10 $\mu$L seed + 45 $\mu$L protein (15 mg/mL) + 45 $\mu$L reservoir. The seeding stock consisted of 12 $\mu$L crushed macrocrystals, 19 $\mu$L protein solution and 19 $\mu$L reservoir. The crystals grew both in the sitting drop and batch setup at 4°C, whereas the batch that was kept at 20°C produced only precipitates. Although the sitting drop and the batch method were both successful, the manipulation of the sample in the sitting drop plates was rather troublesome and therefore this method was promptly dropped. The batch microcrystals were used for the experiments described in **Paper I** and diffracted at 2.27 Å resolution (Fig. 2.3).

From construct 3, we obtained macrocrystals at the same buffer conditions as described above (2.05 Å). We performed a 96 additives screening as well. Two of them, sodium fluoride and ethyl acetate, produced highly diffracting crystals. They diffracted at 1.8 and 1.71 Å resolution respectively. We selected the condition with ethyl acetate as an additive and made microcrystals in batch by mixing 20 $\mu$L seeds, 40 $\mu$L protein (15mg/mL) and 40 $\mu$L reservoir. After 2 days at 4 °C, the crystals fully grew and reached their final size. These microcystals diffracted at 2.3 Å in a synchrotron based serial crystallography experiment (**Paper III**) and 1.7 Å at an XFEL facility (**PaperII**).

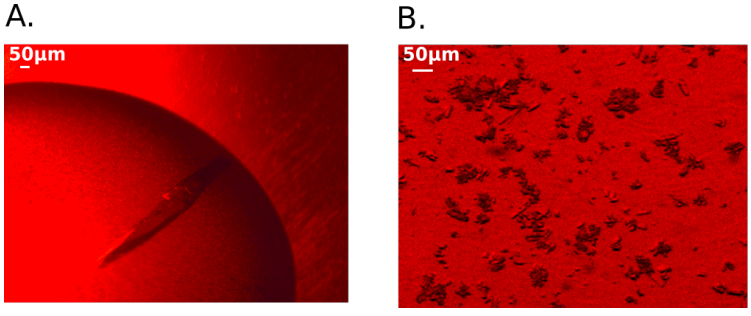


**Figure 2.3:** Macrocrystal (A) and microcrystals (B) of *D.m*(6-4)PL.

## 2.5 Protein and protein crystal reactivity to light

Our aim is to study light induced structural changes in *D.m*(6-4)PL. It is then important to assess that the protein can react to light both in solution and in crystalline form.

We can easily assess the photoswitching properties of the flavoprotein by UV-Vis spectroscopy. From Fig 2.4, we can see the bleaching of the 3 peaks around 400 nm after continuous exposure to 455nm LED light corresponding to a complete reduction of $FAD_{ox}$ to $FADH^{-}$. This behaviour is also maintained when the protein is in crystalline form (**Paper I**)(Fig. 2.4). In addition, we performed a pump-probe experiment in which the protein in solution was excited for 100 ms with a 453 nm LED and spectra were recorded with a 5ms delay. We could evaluate that after 100ms exposure to light, the majority of the FAD was in the anionic radical semiquinone state , $FAD^{\cdot -}$ state **(Paper III)**.

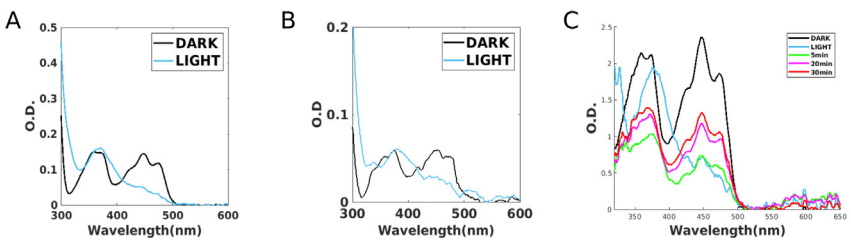


**Figure 2.4:** UV-Vis spectra. The UV-vis spectrum of protein in solution (A) and UV-Vis spectrum of the crystalline form of the protein (B) show that the FAD initial state is the fully oxidized form (black line) and after illumination the FAD gets fully reduced (light blue line). Section C shows the dark reversion of the protein back to its fully oxidized form. The sample was illuminated until the FAD got reduced to FADH- and spectra in dark and anaerobic conditions were taken after 5 min, 20 min and 30 min.

# Chapter 3

# X-ray diffraction, SFX and SSX

We studied the molecular mechanism associated with *D.m*(6-4)photolyase photoactivation by serial synchrotron crystallography (SSX) and serial femtosecond crystallography (SFX). In chapter III, I will briefly describe these techniques and the data analysis process for the determination of the structures in **Paper I**, **Paper II** and **Paper III**.

## 3.1 X-ray diffraction

In the crystalline lattice, planes that cross the lattice points are called *lattice indices* or *Miller indices* and are identified by the three *hkl* indices. A set of parallel *Miller indices* can be seen as a diffractor and hence produces a reflection after x-ray irradiation.

A set of parallel planes *(hkl)* produces a diffracted beam only if the condition described by the *Bragg*'s law is met:

$$2d_{hkl}sin(\theta) = n\lambda \tag{3.1}$$

where $d_{hkl}$ is the spacing between the planes, $\theta$ is the x-rays' incident angle, $\lambda$ is the wavelength of the x-rays and *n* is an integer number.

In other words, if the difference in the path of the reflected rays from the parallel planes corresponds to a multiple of the x-ray wavelength, the reflected rays are in phase. This would lead to constructive interference that results in an amplification of the reflected rays and the generation

of a reflection or *Bragg*'s peak. Hence, each *Bragg*'s peak corresponds to the diffraction from a set of crystal planes defined by the *Miller* indices. The intensity of each reflection is proportional to the amount of electrons/scatterers in the planes and its position is related to the crystal lattice. The diffraction pattern from a protein crystal is the representation of the real lattice in reciprocal space. The relation between crystal real lattice and reciprocal lattice in term of crystal diffraction is described by the *Sphere of reflection* or *Ewald sphere*. According to this geometrical construction, only reciprocal lattice points that are in contact with a sphere of radius $1/\lambda$ (where $1/\lambda$ is the inverse of the x-ray wavelength) can result in a reflection (Fig. 3.1).

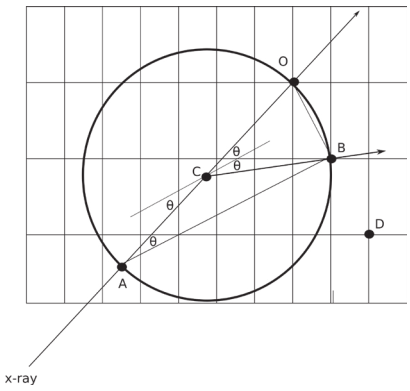


**Figure 3.1:** 2D scheme of the Ewald sphere. In the figure, O is the origin of the reciprocal lattice, C is the center of a circle of $1/\lambda$ radius, P is a reciprocal lattice point. From this construction, we can compute that $\sin(\theta)$=OB/AO with OB=$2/\lambda$ and OB= $1/d_{hkl}$. Hence, Bragg's law can be applied and reflection can be produced when a reciprocal lattice point is on the circle. While rotating the crystal, in respect of the x-ray beam, a new lattice point D can come in contact with the circle and produce a diffracted beam. The beam would diffract at an angle equal to $2\theta$ along the CD direction.

Therefore, in order to record more reflections, more reciprocal lattice points need to be localized on the *reflections* sphere. The strategy is then to rotate the crystal with respect to the x-ray beam. When rotating the crystal, other reciprocal lattice points move and at first diffract weakly (*partial reflections*) until the further rotation of the crystal brings them

on to reflection sphere. It is only then that we have high diffraction and full reflections can be recorded. The *reflection sphere* highlights the importance of the x-ray wavelength and the unit cell length. The shorter the wavelength of x-rays and unit cells is, the higher is the number of reflections that can be measured.

Reflections can be described as structure factors. Structure factors are expressed as Fourier sum in which each element represents the contribution of each atom in the generation of the reflection:

$$F_{hkl} = \sum_{j=1}^{n} f_j e^{2\pi i(hx_j + ky_j + lz_j)} \tag{3.2}$$

In 3.2, $f_j$ is the *scattering function* of an atom *j*; *x, y, z* are the coordinates in real space of the atom *j* and *h,k,l* are the indices of the reflection and frequencies of the diffracted x-ray beam.

Atoms have an electron density, $\rho$, so the above equation can also be expressed using the electron densities:

$$F_{hkl} = \int_x \int_y \int_z \rho(x, y, z) e^{2\pi i(hx+ky+lz)}\, dx\, dy\, dz \tag{3.3}$$

Inverting the above equation shows how we can obtain the electron densities from the structure factors:

$$\rho(x, y, z) = \frac{1}{V} \sum_h \sum_k \sum_l F_{hkl} e^{-2\pi i(hx+ky+lz)} \tag{3.4}$$

where V is the unit cell's volume.

The equation above implies that the determination of the structure factors is necessary for the computation of the electron density. To obtain the structure factors from the experimental data, we need information on the amplitude, frequency and phase of the diffracted rays. The amplitude of a $F_{hkl}$ is proportional to $\sqrt{I_{hkl}}$ (where $I_{hkl}$ corresponds to the intensity of the reflections), whereas its frequency is given by the distance between the planes that generate the reflection ($1/\mathrm{d}_h kl$). The only parameter that is missing and cannot be obtained from the measurements of the reflection intensity is the phase. There are few methods for determining the

phase: isomorphous replacement, anomalous dispersion and molecular replacement (MR). The latter is the most popular and it has been used for resolving the structure of *D.m*(6-4)PL (**Paper I, II and III**). MR method estimates the phases of the structure of interest from the phases of a model structure.

The MR can be based either on the Patterson function [87] or the maximum likelihood method which *Phaser* (a software that we used for phase determination) currently adopts [88]. The maximum likelihood based MR method is a statistical method in reciprocal space. In a simplistic way it operates by moving the provided model in different orientations and positions and giving out the probability of a match between the calculated models' structure factors and the observed structure factors. Then, it ranks the models according to a score system and the solution with the highest score is provided [89].

## 3.2 Data collection and analysis in single crystal x-ray crystallography (MX)

When performing a MX experiment, the crystal is mounted on a support ( i.e. goniostat) and rotated around the $\omega$ axis, normal to the x-ray beam. There are several parameters that can be modified prior data collection: the distance of the detector (which defines the highest resolution limit for your data); the total amount of images to collect and the oscillation range; the exposure time and x-ray transmission; the x-ray wavelength (usually 1Å but it varies in case of recording data for anomalous scattering) [90].

Overexposure of the crystals to x-rays could lead to radiation damage. For instance, one common practice is to increase the exposure time for better signal-to-noise ratio, but that would increase the amount of energy absorbed by the crystals and hence increase the chance of radiation damage which in turn would effectively decrease the data quality. Radiation damages can be classified in two categories: general or specific damages. General damages can be easily spotted during data collection because of the reduction of the reflections intensity and higher level of mosaicity. Specific damages can be detected by visualizing the electron density maps on software like *COOT* [91]. Indeed, we can observe loss of

electron density around aspartates and glutamates due to decarboxylation, around tyrosines as their -OH groups get removed and around methionines where the S—C bond is cleaved [92]. Another secondary effect of x-rays exposure can be observed in proteins with cofactors/prosthetic groups. Water radiolysis induced by x-rays releases electrons and protons which can induce the reduction of cofactors/prosthetic groups [93]. In order to counteract the damages of this ionizing radiation, the experiments are carried out under cryogenic condition implemented by using a cryostream. Such damages would be very localised to the X-ray incident spot and new data can be collected at new spots on the crystal. Hence, the rotation of the crystal is helpful. It was estimated that the damage can spread only by 3 $\mu$m in cryogenic conditions but at room temperature this value increases drastically [94]. A simple way to check whether we expose the crystals to radiation damage is to calculate the dose with a software named *RADDOSE* and check whether or not the dose reaches the limit value of 43 MGy for MX [95].

After data collection, the data needs to be analysed. The steps that one can perform are the following four: spot finding and indexing, parameters refinement and integration followed by scaling and merging of the reflections.

Spots finding consists of determining the number of spots above the background noise, their positions, the number of pixels per spot. From that, the software of choice would try to determine the Bravais lattice and the cell unit parameters (i.e. indexing).

Once the symmetry is determined, the cell unit parameters undergo a refinement process mainly due to uncertainty in the experimental parameters (for example the detector distance and the positions of the detector and the rotation axis for the crystals).

The integration step determines the intensities of the spots by discerning the pixels that correspond to the reflections from the pixels that are caused by background noise. Other problems that need to be considered are pixels that present either extremely high or low counts and pixels that are not working. Usually a mask file takes care of that and of eventual shadows produced by the beam stop or the goniostat.

Due to the fluctuations in the radiation intensity, area of exposure

within the crystals, radiation damage and anisotropy of crystals, measurements are not in the same scale. Therefore, a scaling process is needed. Afterwards, symmetry equivalent reflections are merged [96].

There are some parameters that need to be considered in order to assess the quality of the merged data. The most used ones are the multiplicity, $CC_{1/2}$, *CC** and the signal to noise ratio (i.e. $I/\sigma$). Multiplicity gives how many time the measurements have been taken. This parameter is correlated to the signal to noise ratio. The higher the number of repeated measurements is, the lower the standard error of the measurements gets and hence the higher is the $I/\sigma$ value. Another parameter that depends on the signal to noise ratio is $CC_{1/2}$ which is the Pearson's correlation coefficient ($CC$) between intensity of two half datasets. $CC_{1/2}$ values range from 0 to 1, with 1 corresponding to highly correlated data [97]. *CC** is derived from $CC_{1/2}$ and carries the same information as $CC_{1/2}$ itself [98].

## 3.3 SFX and SSX

The development of x-ray free electron laser (XFEL) has paved a new era for time-resolved studies. Its short pulses of 40 fs allows us to investigate ultrafast events in the range of hundreds of fs and ps. Although the XFEL pulses are extremely short, they contain $10^{12}$ photons and can reach an intensity up to $10^{17}$Wcm$^2$, completely destroying the sample after exposure to x-rays. However, we are able to record diffraction patterns before the sample is completely destroyed [99]. The continuous destruction of the crystal sample requires a constant replenishment of fresh crystals and therefore data are acquired from a series of crystals. Many delivery systems have been the developed over the years. Some require that the crystals are extruded from an injector, whereas in others the crystals are fixed on a solid substrate.

Inspired by the success of SFX, serial synchroton crystallography or SX was developed. In the third generation synchrotron where the beam is monochromatic, the x-ray pulse can reach $10^{12}$ photons/s when microfocused. To achieve that flux, the exposure time is increased and the resulting pulse is longer than the XFEL pulse. As a consequence, synchrotron radiation can be used for time-resolve studies on the ms time

scale. For better time resolution, an alternative is to use the fast pulse (100ps) of a polychromatic pink-beam [100].

### 3.3.1 Sample delivery in SFX and SSX

For serial crystallography, the delivery of the crystals can be achieved in two ways: either the sample flows from an injector or the sample is laid on a chip (fixed target) [101, 102]. I will shortly describe the jetting systems since one of them (the LCP injector) was picked for our experiments in **Paper I**, **Paper II** and **Paper III**.

The GDVN (Gas Dynamic Virtual Nozzle) injector is one of the most used injectors for SFX experiments. In this setup, crystals in solutions are flowing through a capillary. The jet is then focused to create a stream of 2–6 $\mu$m diameter. To generate a perfect jet, the sample is pumped at a flow rate of 10-40 $\mu$L per minute. The necessity of a flow rate this high requires hundred and hundred of mg of protein to purify and crystallize. Therefore, new ways of reducing sample consumption were in high demand [103]. In this context, the LCP (lipidic cubic phase) injector can be employed [104]. When using this type of injector, the sample is diluted by mixing it with a medium. Many viscous media are available and crystal can be mixed in lipid cubic phase (LCP), agarose, grease, vaseline, hyaluronic acid and hydroxyethyl cellulose (HEC) [105–109]. The carrier choice is mainly associated with the survival chance of the crystals embedded within the material. In our case, crystals could survive in HEC but not in grease (Fig. 3.2).

The crystal sample embedded in a matrix is loaded in a reservoir, on top of which a teflon ball (or two teflon balls) is placed. A piston connected to a HPLC pump plunges upon the teflon ball(s) and extrudes the sample. A gas stream (either helium or nitrogen) flows coaxially to the crystals slurry to maintain the stream perpendicular to the x-ray beam. A combination of helium and a catcher can be advantageous in order to not disrupt the sample stream [104].

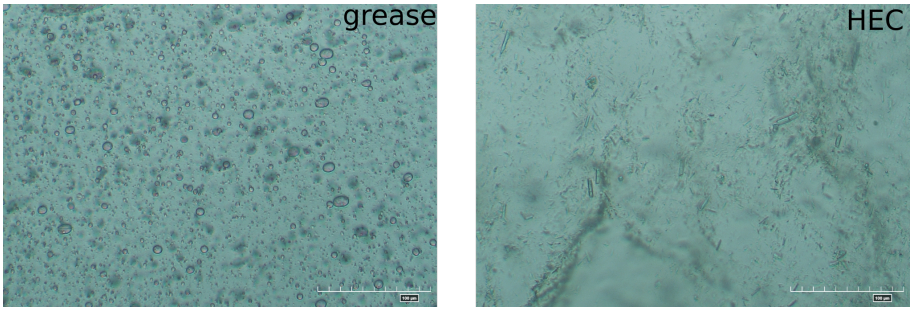


**Figure 3.2:** Images of crystals mixed in grease (left panel) and 22% HEC (right panel). Overnight, the crystals survived in HEC and melted completely in grease.

### Pump-probe experiment

Time-resolved experiments are a good tool to study proteins in motion. SFX or SSX can be chosen according to the type of event in consideration. The short pulse of XFEL allows us to study fast processes in the fs-ps time range whereas with the longer synchrotron pulse it is possible to study late events in the $\mu$s-ms time resolution (Fig. 3.3).

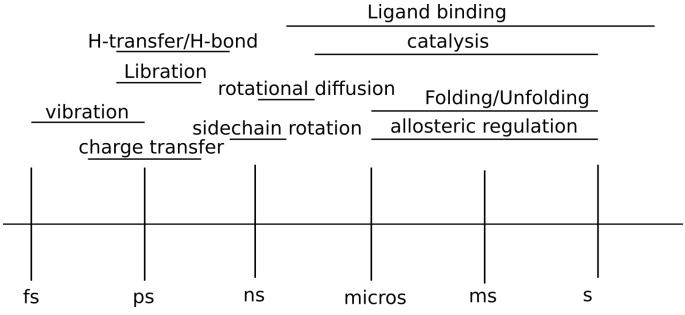


**Figure 3.3:** Timescale of protein motions and events.

In pump-probe experiments, a reaction is triggered by the *pump* (e.g by a light pulse or by mixing the crystals with the ligand of interest). As the reaction evolves over time, the probe (i.e. the x-ray beam in our experiments) hits the sample at different time delays and produces diffraction patterns (Fig. 3.4). In this way, we are able to capture the structure

intermediates at different time points and reconstruct how the protein "moves" during and after its activation.

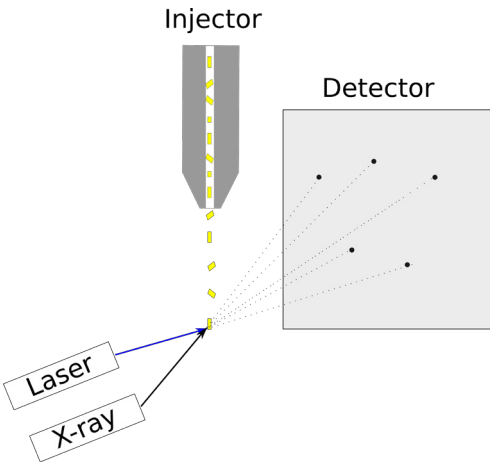


**Figure 3.4:** Set-up for light triggered time-resolved studies on microcrystals.

## 3.4 SFX data analysis

During a serial crystallography experiment, we collect thousands and thousands of snapshots every time the probe hits a crystal. The number of diffraction patterns that we are able to collect from a reservoir is dependent on the x-ray pulses frequency, the read-out frequency of the detector and the sample flow. Due to the high frequency of the x-rays and the detector, the images acquired are mainly empty. Therefore an initial procedure of "hit finding" is implemented to distinguish the empty frames from the ones that contain *Bragg*'s spots. In many beamlines, this data reduction task is performed by *Cheetah* [110].

The following steps consist in the indexing and integration of the reflections by *indexamajig* in *Crystfel* [111]. *Indexamajig* calls out indexing programs such as *XDS* [112], *Mosflm* [113] and *Dirax* [114]. If the indexing is not correct or the indexing rate (i.e. the ratio between the number of indexed frames and the total number of frames) is too low, a refinement of the "peak-finding" parameters and of the detector's geometry can be implemented. For SSX experiments, the optimization of the geometry of the detector consists of optimizing the detector camera length and the detector offset with respect to the beam (*detector-shift* in *Crystfel*). For SFX, a multipanels detector is used and a more complex refinement is performed by optimizing the position of each panel (*geoptimizer* in *Crystfel*) [115].

Afterwards, the data are merged. In SX, the crystals are not rotated and it is not possible to collect full reflections. The intensity of full reflections is obtained by merging the data with the *Monte Carlo* method which consists in determining the mean intensity for each measurement [116].

Several figures of merit can be considered to assess data quality. Other than $CC_{1/2}$ and *CC** mentioned before, in the SFX community one parameter that is widely used is the $R_{split}$. For the calculation of $R_{split}$, the dataset is split into two different sets, the two sets are then merged separately and the two intensities lists are compared. The higher the agreement between the two sets is, the closer to 0 is the value of the *R-factor* [111].

## 3.5 Electron density maps

For the refinements of structure, the electron density map from the structure factors is used to guide the crystallographer in the the process of building the protein structure. At this step, another *R-factor* is considered to estimate the agreement between the calculated structure factors from the model ($F_c$) and the observed structure factors ($F_o$):

$$R = \frac{\sum ||F_o| - |F_c||}{\sum |F_o|} \tag{3.5}$$

According to the formula, a better fitting can be achieved by minimizing the difference between the two structure factors and therefore by reducing the value of the *R-factor*. However, the evaluation of the model cannot be based exclusively on this *R-factor* since it can be easily altered by adding more water molecules and hence by overfitting. In parallel to this *R-factor*, $R_{free}$ factor must be considered. The $R_{free}$ factor is an *R factor* computed in respect of a set of reflections that are excluded from refinement. Therefore, any overfitting operation won't lead to any changes in the $R_{free}$ but only to a greater discrepancy between the two *R-factors*.

In some circumstances, the model building process becomes difficult due to either a lack or the weakness of the electron density around some residues and/or ligands. One way of refining these regions in the most accurate way is to compute *omit maps*. *Omit maps* are maps that are used to support the presence of structural features (e.g. a loop, a residue or a ligand) without bias coming from the phase construction or from the model itself. Several omit map methods can be used. The simplest consists in calculating the electron density map after removing the features under analysis. Two other examples are the *composite omit map* and the *POLDER* omit map (**paper I**) (Fig. 3.5). In the first method, the map is generated by omitting random portions of the model and the resulting omit maps are then assembled together. In the *POLDER* omit map, not only the selected region is excluded but also part of its surrounding area is removed and excluded from the bulk solvent mask calculation. By doing this operation, the electron density around the selected area gets clearer thus making the model building process way easier [117].

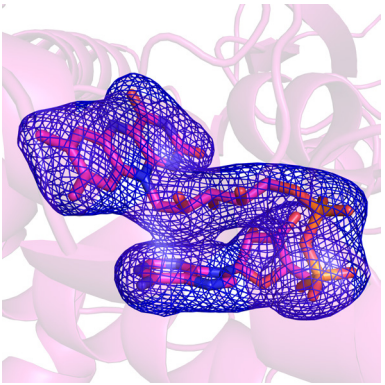

**Figure 3.5:** FAD polder maps countoured at 3$\sigma$ from the room-temperature structure in **Paper I**.

### 3.5.1 Difference electron density map

Time-resolved SFX and/or SX can be used to characterize proteins conformational changes upon light activation. An efficient way to assess the differences between the initial state ("dark" state) and the final state ("light" state) is to compute a difference electron density map from the dark and light structure factors (${F_{obs}}^{light}$-${F_{obs}}^{dark}$). Prior to the calculation of ${F_{obs}}^{light}$-${F_{obs}}^{dark}$, the ${F_{obs}}^{light}$ and ${F_{obs}}^{dark}$ are scaled with respect to the calculated structure factors from the dark model ($F_{calc}$) and then to each other. Once the structure factors are scaled and the ${F_{obs}}^{light}$-${F_{obs}}^{dark}$ is computed, the amplitudes difference is weighted with a Bayesian weight to reduce the impact of the outliers and enhance the signal-to-noise ratio [118, 119]. Difference electron density maps can be easily visualized in *COOT* and are contoured at an appropriate RMSD (root-mean-square deviation) to avoid to take in consideration signals derived from the background noise. The difference electron density could be either positive or negative. Where the difference is negative, the structural details present in the dark model are absent in the light structure. The position of the nearby positive features indicates where the structural details should be oriented or positioned in the light structure.

### 3.5.2 1-D representation of difference electron density

When comparing difference electron density maps in *COOT*, it is not easy to keep track of the changes that might occur within the protein and some difference signals can be omitted by mistake. A convenient tool to track and plot the difference signals in one dimension has been developed by Wickstrand et al [120]. The algorithm defines a 2 Å radius sphere around each atom position in the resting state model. Then, the difference density amplitudes are extracted at each position of the grid defined inside the sphere. The amplitudes are excluded if they fall under a threshold that the user defines (in our case, the threshold was set at $3.2\sigma$ (**PaperIII**)). Finally, the negative and positive features are calculated for each sphere and plotted. This tool is extremely helpful for time-resolved data analysis. Indeed, it can help you to follow the evolution of difference signals around the residues of interest over the course of time. In this way, we can distinguish the first events from the latest.

### 3.5.3 Light extrapolated maps

Plotting and observing the difference electron density maps can help us to study and understand the light-triggered structural rearrangements in light responding proteins. However, the final goal is to refine a model of the light activated protein at different time points and accurately describe protein motions. The refinement of the light structure is not straightforward since the experimental light data is skewed towards the dark data information. Indeed, within the crystal, only a fraction of the proteins gets activated while the predominant part would either remain or go back to the dark conformation. The approach that we employed (**Paper II** and **Paper III**) consists in the calculation of the light extrapolated structure factors from the difference between light and dark structure factors according to the following formula:

$$|F_e| = \frac{1}{A}(|F_{obs}^{light}| - |F_{obs}^{dark}|) + |F_{calc}| \tag{3.6}$$

where A represents the activation level, defined as the molecules in per cent that are light activated [121–123] and $F_{calc}$ are the calculated structure factors from a refined dark model. The phase is retrieved from the refined dark model whose structure factors were used to compute the light extrapolated structure factors. The dark model is then visualized in *COOT* and the light extrapolated maps are plotted against the dark model. The map is used as a reference in refining the light structure in real space.

After the refinement, the light structure is validated by visual comparison of the observed difference map ($F_{obs}^{light}$- $F_{obs}^{dark}$) with a calculated difference map obtained from the calculated structure factors of the light and dark models ($F_{calc}^{light}$- $F_{calc}^{dark}$). Another tool that we implemented to select the most accurate light structure is to calculate the Pearson Correlation Coefficient (*PCC*) between the observed difference map and the calculated difference map for each structure.

# Chapter 4

# The early and late events in *D.m*(6-4) photolyase photoresponse

We conducted a few serial crystallography experiments described in detail in **Paper I**, **Paper II** and **Paper III**. In this Chapter, I will present the main results from each paper and describe the structural rearrangements of *D.m* (6-4) photolyase during charge transfer.

## 4.1 Room temperature structure of *D.m*(6-4) photolyase

In **Paper I**, we present new reservoir conditions for *D.m*(6-4)photolyase macrocrystals. The crystals were grown in a hanging drop plate with a reservoir of 0.2 M lithium sulfate monohydrate, 0.1 M bis-tris (pH=6.5), 25% of PEG3350 and 4% polypropylene glycol P 400. Data were collected at a synchrothron (BioMAX in Sweden) and analyzed with the XDS software package. The structural analysis confirms what was previously observed by Maul et al. [75]. Indeed, the overall 3-D structure of *D.m*(6-4)PL presents the typical architecture of a CPF member with a N-terminal $\alpha/\beta$ domain and a C-terminal $\alpha$ domain (Fig.4.1).

The microcrystallization batch protocol was adapted from the methods reported by Claesson et al. [85]. We introduced an extra step of seeding to improve the nucleation rate. The microcrystals were homogeneous

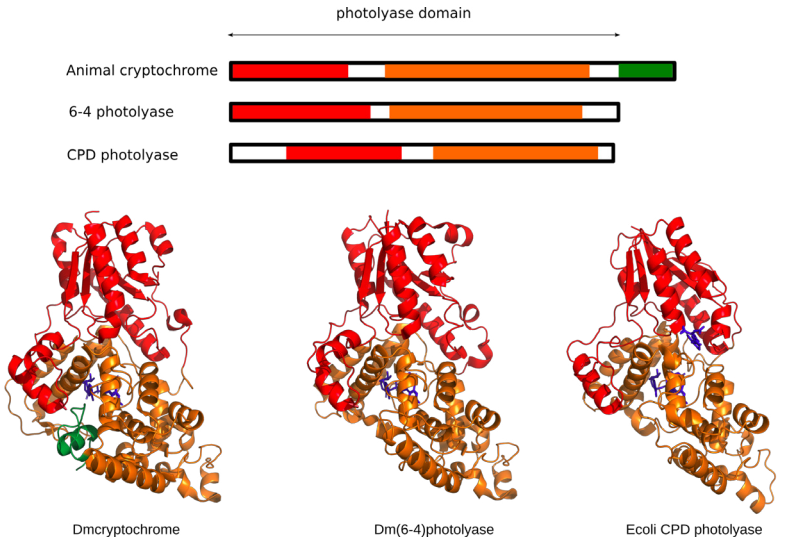


**Figure 4.1:** 3D-models of *D.m*Cryptochrome [42], our cryogenic model of *D.m*(6-4)photolyase and *E.coli* CPD photolyase [40]. The $\alpha/\beta$ is depicted in red, the $\alpha$ domain in orange and the CCE in *D.m*Cryptochrome in green. The FAD is portrayed in dark blue.

in size distribution (20-40 $\mu$m) and hence optimal for serial crystallography experiments with a viscous injector as a delivery system. The data were collected at SACLA (spring-8 angstrom compact free electron laser), an XFEL facility based in Japan. From the data, we refined a structure at a resolution of 2.27 Å and it was the first (6-4)photolyase structure solved at room temperature and in a SX setup.

The room temperature structure was compared to the previously resolved cryogenic structure. We could observe that the structure at room temperature maintains the same features as the cryogenic one. We computed the RMSD on the residues main chains and the side chains to detect where the possible differences might occur. Overall, the main chains RMSD is only 0.35 Å indicating that the structure is preserved at room temperature. The results from the analysis of the RMSD on the side chains are in line with what we could expect from a room temperature data collection. Indeed, we observe differences on residues located on the protein surface or in loop regions which can be attributed to a thermal effect (Fig.

4.2).

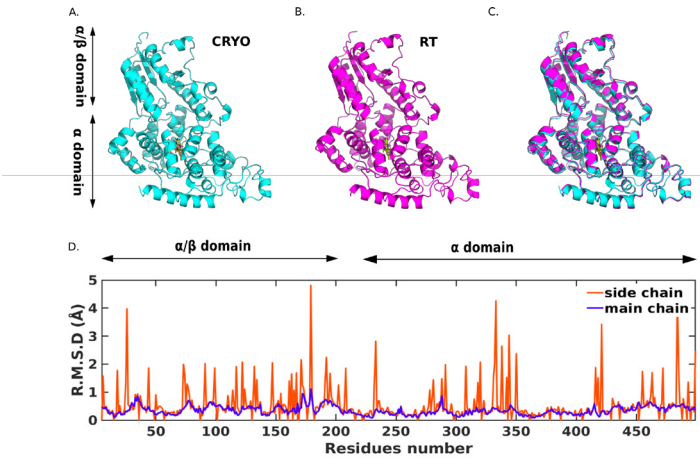


**Figure 4.2:** Overview of the 3D structure of Dm(6–4)PL at cryogenic (A) and ambient temperature (B). The cryogenic structure of *D.m*(6–4)PL was solved at 1.79 Å resolution (PDB ID: 7AYV) whereas the room temperature structure of *D.m*(6–4)PL was solved at 2.27Å resolution (PDB ID: 7AZT). In (C) a Superimposition of PDB entry 7AYV and 7AZT was performed to ease the comparison between the two models. In (D) RMSD of the main chains (blue) and the side chains (orange) of the room-temperature structure in respect of the cryo-structure used as a reference.

## 4.2 *D.m*(6-4)photolyase primary structural photoresponse

In **Paper II** (manuscript), we present the very first structural response of *D.m*(6-4) photolyase to the photo-induced reduction of FAD to $FAD^{-}$. In the paper, we show how in response to this first step of reduction water molecules, the conserved N403 and the conserved salt bridge between R368 and D397 rearrange.

The data from **Paper II** were acquired at SwissFEL where we collected diffraction patterns in a pump-probe setup. Firstly, dark data were

collected and then we proceeded to collect data at different time delays (400fs, 1ps, 2ps, 20ps, 300ps and 100$\mu$s) in respect to a 474 nm laser.

From the structure factors of the dark and the lights datasets, we computed the difference electron density maps (DED maps) and the light extrapolated maps for each time points. The extrapolated light maps were then used to refine the light models at 400fs, 1ps, 20 ps and 300 ps. The structures refined from the dark and light structure factors were employed for the computation of the calculated difference electron density maps that were used as a validation tool for our light models.

The DED maps show strong signals around N403 (Fig. 4.3, features I and II) from 400 fs up to 300ps. From 400 fs to 20ps, we observed a rotation of the N403 that places the N403 amino group closer to the FAD N5 and moves the carbonyl group away from it. At 300ps, the rotation of the N403 suggests that the amino group of N403 goes back to the dark position, whereas the carbonyl group is maintained far from the FAD N5.

In proximity of the FAD, we could observe a positive DED feature at 2 ps, 20 ps and 300 ps (feature V, Fig. 4.3). We attributed this feature to a water molecule that can potentially stabilize the $FAD^{\cdot -}$ by moving between the FAD N5 and the N403 and establishing a hydrogen bond with both of them. We modelled a water in that position for the 2 ps, 20 ps and 300 ps structures and computed the Pearson correlation coefficient between the calculated and observed DED maps for each time points. The PCC value confirmed the presence of a water only for the 2ps structure. However, the positive DED could be reproduced (Fig. 4.4, panel E) and we therefore suggest that a water could move between the FAD N5 and N403 to stabilize $FAD^{\cdot -}$.

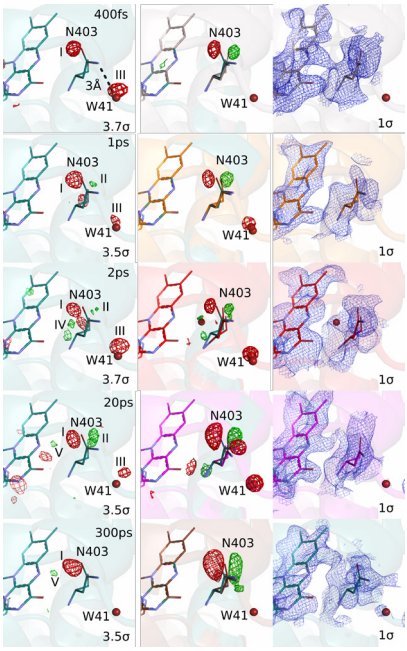


**Figure 4.3:** Observed difference electron density maps (left column), calculated difference electron density maps (middle column) and extrapolated electron density maps plotted on the FAD, N403 and water41 region.

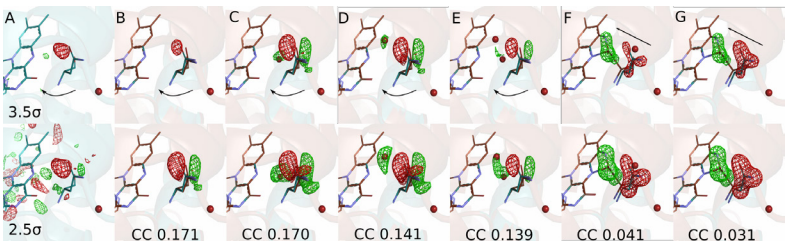


**Figure 4.4:** In A, the observed DED map related to the 300 ps dataset is shown. In B, C, D, E, F, G alternative models for N403 and nearby water molecules are depicted. For each model, the calculated DED maps are plotted against the refined light structures. The Pearson correlation coefficients were also computed and reported at the bottom of each panel.

The DED maps from 400 fs to 20 ps showed a negative feature around the conserved D397-R368 salt bridge. In order to follow the evolution of the DED signal from D397 over time, we implemented the method developed by Wickstrand et al, [120]. The data showed that the signal peaks at 2ps, it is stable at 20 ps and then decays already at 300 ps (Fig. 4.5). From the comparison of the refined structures and the calculation of the distance between D397-R368, we can conclude that the salt bridge weakens and we attribute that to a change in the FAD charge.

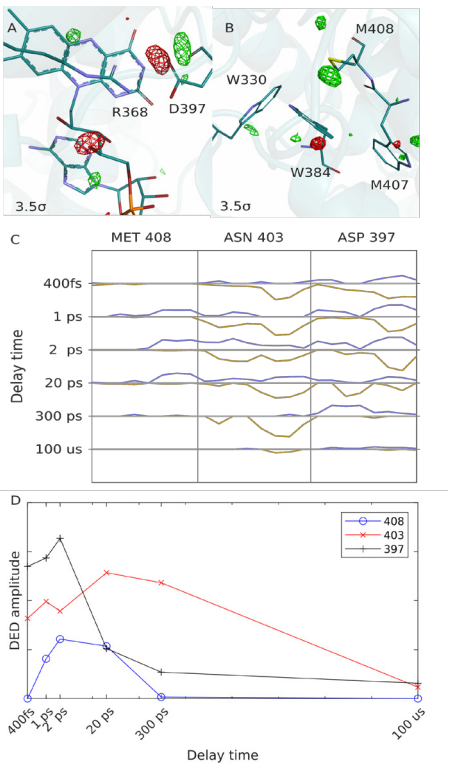


**Figure 4.5:** Observed difference electron density maps (DED maps) around D397 and R368 at 2 ps (A) and around M408 at 20 ps (B). (C.) 1D-representation of the DED on M408, N403 and D397 at different time points. The difference density amplitudes were integrated within a sphere of 2Å radius at each atomic position for values greater than $3.2\sigma$. D. Time-evolution of DED over the side chains of M408, N403, D397.

Around the FAD, we could observe a negative DED at 20ps (Fig. 4.6) and we suggest that it is due to activation of an alternative electron transfer route that takes place within 20ps [65].

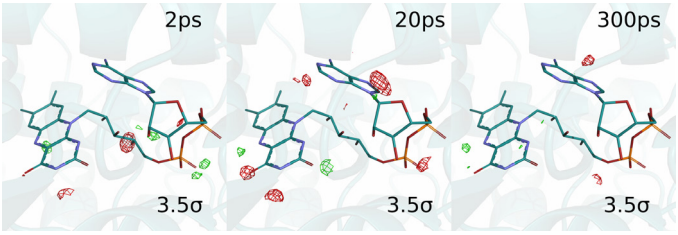


**Figure 4.6:** Observed difference electron density maps around the FAD at 2ps, 20 ps and 300 ps

Finally we examine the tryptophans involved in the electron transfer. We couldn't observe any structural changes that could be associated with the first electron transfer from W407 to the FAD. That could be related either to the rigid surrounding protein environment or to a fast electron transfer from W384 to W407. From 1ps to 20ps, we detect a positive DED on a conserved methionine (M408) near the second tryptophan of the tetrad (W384) (Fig. 4.5). We believe that this positive feature could be an indication that W384 has been oxidized and that the tryptophan remains oxidized for 20ps.

At 100 $\mu$s, we could observe DED signals around the last tryptophans of the tetrad (W381), N490, M494 and P329 (Fig. 4.7 ). We believe that the observed DED signals are indications of the involvement of W381 in the electron transfer. We also think that these changes are brought by the breakage of the hydrogen bond between P329 and W381 (**Paper III**). The DED signals suggest that W381 and N490 are moving closer to each other and are interacting through a hydrogen bond. The hydrogen bond between W381 and N490 suggests that W381 didn't get deprotonated yet and that the tryptophan is in the cationic radical state ($W381H^{+}$).

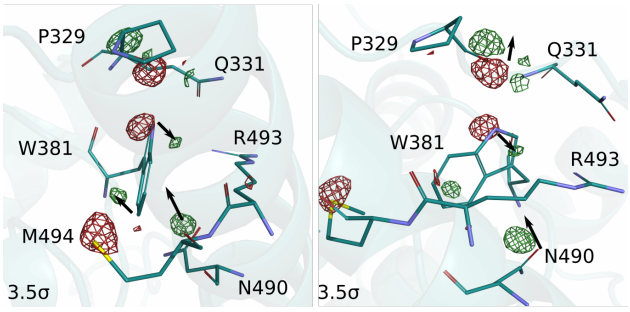


**Figure 4.7:** Observed difference electron density maps around the W381, P329, M494, N490.

In conclusion, we show that in the first 300ps from $FAD^{\cdot -}$ generation, the N403 change its orientation relatively to the FAD and that the D397-R368 salt bridge weakens within 20 ps. Moreover, we show the protein adaptation to the formation of the second radical tryptophanyl takes place in tens of ps and that adaptation is related to M408. Finally, we propose that the fourth radical tryptophanyl forms at 100 $\mu$s and can be stabilized by the formation of a hydrogen bond with N490.

## 4.3 D.m (6-4)photolyase photoresponse in ms time scale

In **Paper III**, we present the structure of *D.m*(6-4) photolyase in its radical pair state ($FAD^{\cdot -}$-$W381^{\cdot}$) captured by serial crystallography. We observed that N403 moves towards the $FAD^{\cdot -}$ establishing a hydrogen bond with it. Moreover, we could observe that residues around W381 moves in response to the formation of the radical $W381^{\cdot}$.

The data from **Paper III** were acquired at SLS (Swiss Light Source in Switzerland) where we performed a steady state experiment. In such setup, we collected diffraction patterns from crystals that were continuously exposed to a blue laser light. We could estimate from the flow rate of the sample that the crystals were probed by the x-ray after 300 ms from light exposure.

At first glance, we could observe a weak signal from the FAD. Although the signal was weak, it was above the noise threshold. Prominent features could be seen around the last tryptophan (W381) of the conserved tetrad of tryptophans involved in the electron transfer (Fig. 4.8).

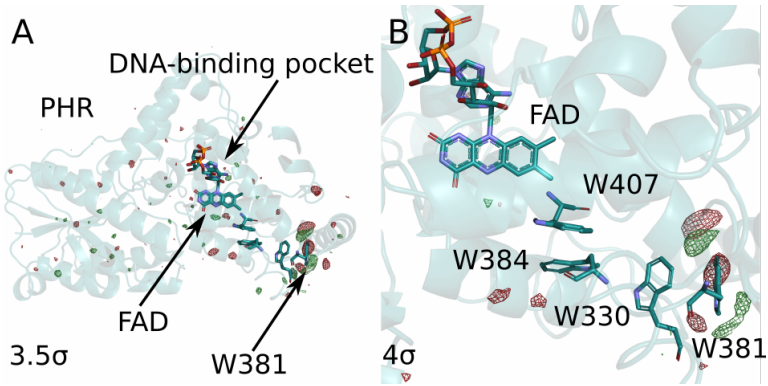


**Figure 4.8:** A) Positive (green) and negative (red) electron difference densities in *D.m.*(6-4) photolyase are shown and plotted against the dark structure (PDB ID:7QUT). (B) The same data are shown for the tryptophan tetrad and the FAD

We modelled the structural changes by real space refinement on 2Fe-Fc map computed by extrapolation of the light structure factors with an

activation factor equal to 14%. The accuracy of light state structure was evaluated by comparing the observed difference map with the calculated difference map (Fig. 4.9).

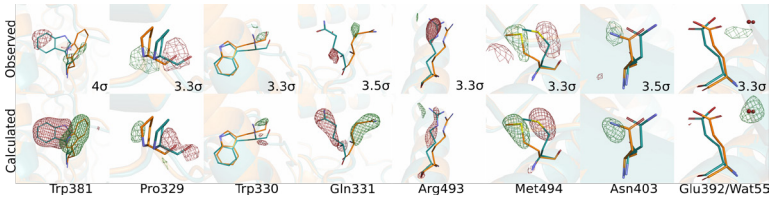


**Figure 4.9:** Comparison between the observed and calculated difference electron density maps for the residues: W381, P329, W330, Q331, R493, M494, N403, water55.

In the FAD-binding region, we could observe positive features at the position of the FAD and water 55 (Fig. 4.10). Moreover, we couldn't observe any difference electron density signal that can be attributed to the bending of the FAD.

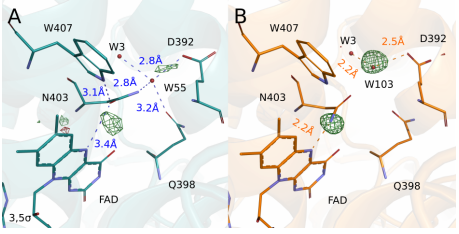


**Figure 4.10:** Comparison between the observed (A) and calculated difference (B) electron density maps within the FAD binding pocket

From Fig. 4.10, we can observe that at first that N403 establishes a hydrogen bond to water 55, Q398 and to the first tryptophan of the tetrad (i.e. W407). Upon illumination, this hydrogen bond network breaks. As a result of the breakage of the N403-W407 hydrogen bond, N403 gets closer to the FAD-N5 as suggested by the positive feature between the FAD and N403 and the extrapolated map (Fig. 4.11). We hypothesize that the asparagine flips and orients the side chain amide group towards the $FAD^{\cdot -}$ and establishes a hydrogen bond with $FAD^{\cdot -}$-N5 thus stabilizing its negative charge.

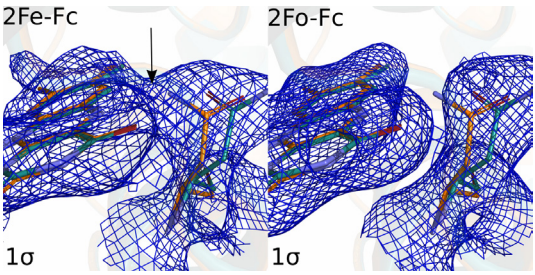


**Figure 4.11:** 2Fe-Fc map from the extrapolated structure factors (on the left) and 2Fobs-FC map computed from the dark structure factors (on the right panel)

In addition to the breakage of the hydrogen bond between N403 and W407, we can point out that the hydrogen bond between W407 and water55 breaks too. This allows the water to move away from Q398 and allows it to establish a stronger hydrogen bond with E392 and water3.

In the C terminal region, we could observe difference signals around W381, P329, R493, M494, and Q331. The comparison between the dark and the light structure suggests that W381 rotates about 34° towards the solvent. We estimated that the solvent accessible area increases from 2.1 $Å^2$ in the dark to 51 $Å^2$ in the light. The movement of the indole group of W381 also increases the distance between the FAD and W381 itself thus slowing down the chances of charge recombination (Fig. 4.12).

From the dark and light structures comparison, we could see that the hydrogen bond between W381 and P329 breaks, resulting in a displacement of the P329 itself of about 0.7 Å. Additionally, W381 and Q331 are not interacting through a hydrogen bond in the light as compared with the dark. As a consequence, the side chain of Q331 moves out towards the solvent.

We believe that the movements of the M494 and R493 are results of the structural rearrangements described above.

Overall, we think that the photo-induced oxidation of W381 starts with the breakage of the hydrogen bond with P329 and then with Q331. These changes would allow W381 to have more access to the surrounding solvent.

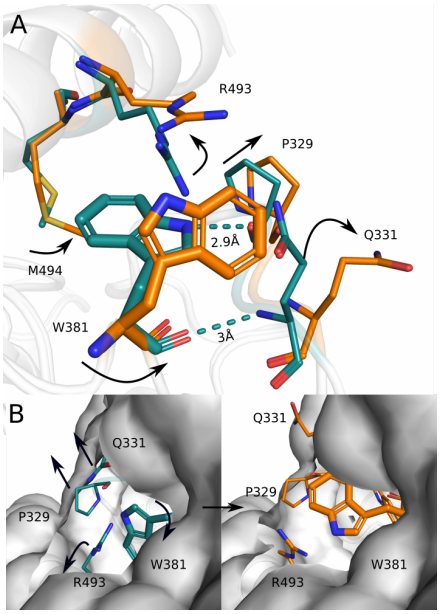


**Figure 4.12:** In A. the superimposition of the dark (blue) and the light (orange) structures around Trp381 are depicted. In B Surfaces of the dark and the light structure are shown.

We couldn't detect any possible residues around W381 that could be involved in the deprotonation of $W381H^{\cdot+}$ and we therefore conclude that the solvent could partake in that process.

In conclusion, we presented a structure of a photoactivated (6-4)photolyase in the $FAD^{\cdot-}$-$W381^{\cdot}$ state. We showed that small rearrangements occur around the FAD and W381 areas and these can contribute to the stabilization of the radical pair.

# Chapter 5

# Concluding remarks and future perspectives

In this thesis, I showed a way of producing highly diffracting crystals of *D.m*(6-4)photolyase. We used these crystals to study the early and the late events of photolyase photoresponse. In particular, we could observe movements of residues around the chromophore region and around the conserved tryptophans through which the electron is hopping.

However, the photoactivation mechanism requires further studies. X-ray data related to later time points are necessary to study the structural changes associated with the electron transfer on the third tryptophan. In addition, time-resolved x-ray crystallography studies on the photoactivation steps involving the $FADH^{\cdot}$ and tryptophanyl radicals haven't yet be performed in (6-4)photolyases.

The elucidation of the structural changes associated with the photoactivation mechanism can help us to understand how the protein is primed for DNA-repair. Moreover the homology of (6-4) photolyases with animal cryptochromes can lead to a better understanding of the the molecular mechanism behind cryptochrome photoactivation.

These studies also have a direct impact on the treatment of diseases that are associated with the presence of DNA lesions that photolyases can repair [124, 125]. A better understanding of the photoactivation mechanism could potentially be helpful in engineering photolyases and making them a more efficient tool for repairing the DNA and preventing such diseases.

# Chapter 6

# Svensk sammanfattning

Fotolyas är ett enzym som katalyserar ljusaktivering av UV-bestrålat DNA. Genom att bryta en kol-kolbindning i dimerer av pyrimidin-pyrimidon hos DNA reparerar fotolyas UV skadade DNA med energi från blått ljus.

Denna avhandling fokuserar på att undersöka de strukturella förändringar som sker i kromoforen FAD och i själva (6-4)fotolyas efter att FAD träffats av blått ljus. För att kartlägga strukturen av fotolyas på atomnivå användes en metod som heter röntgenkristallografi. Först produceras proteinkristaller som sedan belyses med stark röntgenstrålning, varpå en del av strålningen reflekteras och detekteras. Från de detekterade reflektionerna kan man försöka att räkna baklänges för att lista ut vilka atomer röntgenljus har reflekterats från. På så sätt kan man kartlägga positioner av atomerna och pussla ihop en tredimensionell bild av proteinet. Dessutom, genom att använda sig av två olika typer av tidsupplöst kristallografi, SSX och SFX, kan man följa hur olika atomer i fotolyas förflyttar sig under tiden efter blått ljus träffar kromoforen.

Denna information ger oss insyn i hur fotolyas skördar energi från blått ljus och hur det sedan använder energin till att reparera skadat DNA. I bananflugor jobbar fotolyas konstant med att leta efter UV-skadat DNA och laga det så fort det upptäcks. Men i människor lyser fungerande fotolyas med frånvaro. Man skulle kunna tänka sig att framtidens solkräm kan innehålla tillsatt fotolyas som är funktionellt och effektivt lagar vårt UV-skadade DNA. Då kan man sola hur mycket man vill utan att vara orolig för hudcancer.

# Chapter 7

# Acknowledgments

Four years have already passed and I cannot believe that my moment has come. Lundberg is really a magic place and I felt welcomed since day one. It was really a pleasure to meet you all! I have a long list of people I'd like to thank and I'll try to keep it short.

First of all, I'd like to thank my supervisor, **Sebastian**. Thank you for accepting me in your group and I still cannot believe you hired me, a biologist. I hope it was worth it. Also, thank you for introducing me to crystallography and to photolyases's world. Your drive and commitment are inspiring. Even in the darkest moments and we had a few with photolyase, you were always positive. I must say that producing and studying photolyase was not a walk in the park but I think we made something out of it! I'd like to also thank my co-supervisor **Weixiao**, thank you for the support, guidance and help. I'll cherish in my heart all the frantic phone calls about not having crystals just few days before every beamtimes. Also, we had a lot of fun during beamtimes. **Amke**, the last old generation Westenhoff's standing. Although we are far now, we had so much fun together. Thank you for all the spectroscopy measurements that I couldn't do by myself and thank you for supporting and withstanding me. Also, my spotify playlist is full of Amke's songs. **Lidija, Taru, Jennifer, Szabolcs, Petra, Leonardo, Massoud and Madan**, I hope you will have fun in this group and I wish you the best. Lastly, I just want to thank former member of Sebastian's group: **Leo**, thank you for the precious advises on åktas and on mosquito and thank you for introducing me to the lab.**Elin**, we are still using your pymol scripts as templates and thank you for the funny moments and laughter. **Linnea**, thank you for teaching me western

blot. Although now i really hate it.

I'd like to thank my examiner,**Richard**, thank you for supporting me but most importantly thank you for the funny moments during beer club. Also, I am grateful to the remaining PIs **Gisela**,**Bjorn**, **Kristina**, **Gergely**, **Johanna**, **Julia** and **Irena**. Thank you for creating such a lovely and inspiring environment, here in Lundberg. Keep up with the great work!

Now it is time to thank all the other people from the second floor. First of all, **Ann**, you are my rock. I cannot thank you enough for all your support and honest opinions. Your inquiring eyes will lead you far and you will be successful. Don't forget to free Dobby eventually. **Lucija**, you are incredible. Thank you for the fun we had together in and out Lundberg. Hvala, for helping me in the time of need. **Gio**, I have two words for you:5 minuti?**Per**, you are the kindest British person ever!**Greger**, the healthy guy. I should learn one thing or two from you. **Adams**, thank you for being patient with me when I was completely occupying calc1 and calc2. **Arpitha**, the little boss. You are so lively and bubbly. Maybe one day you can write a poem about Lundberg. **Leona**, good like with the worms!

I'd like to thank all the Brandeneers (is it the correct spelling?) **Owens**, my favourite office mate. you bring happiness everywhere you are going. **Doris**, I am still surprised of your knowledge about italian music from the 80's. **Andreas**, thank you for your inappropriate jokes . **jonathan**, akta 2 is waiting for you. **Gabrielle**, good luck with your PhD. you will enjoy Lundberg.

I'd like to thank the aquaporins club:**Jessy**, my spatzi, the lab is empty without you. **Flo**, aka ciccio bello. The fermentors are waiting for you, come back!

I am grateful to Gergely's squad. **Laras**, the fashionable piano player. Thank you for your support and for the flavourful candies. **Torbjörn**, good luck with your Phd, you'll have fun. I cannot think about Gergely's group without mentioning **Majo** and **Maja**. **Majo**, thank you for teaching me how XDS works, to help me during remotely data collection and thank you for you kindness. **Maja**, thank you for lending me your cat whiskers and all the chats at every defense.

Moving to the first floor or should I say dungeon? I'd like to thank. **Yosh**, you are so hilarious. I'll miss your sarcasm and the good coffee. **Yilber** and **Jens**, you are the lives and souls of the party. **Hanna**, good

luck with everything. **Filippo**, the lundberg hipster. Good luck with your football matches. **Damasus** and **Emelie**, We made it! (almost) and my dear **Lisa**, aka the PCR goddess, how much fun we had!!!! **Katharina**, thank you for the very light conversations we always have and for Logan's whiskers.

**Tinna**, lil mama. Thank you for helping me for the planing of the PSI beamtime but most importantly thank you for all the amazing morning conversations. They are not quite the same since you left.

and thanks to **Bruno**,**Lars** and **Valida**. The lab will stop working without you.

Finally I'd like to thank my family for supporting me and encouraging me with everything I wanted to do.

I think I cover everyone in Lundberg and If i didn't I am truly sorry. You all are amazing people and made this journey an amazing experience

I have just one last thing to say: byeeeeeeee.

# Bibliography


[1] X. Liu, Y. Li, and S. Zhong, "Interplay between light and plant hormones in the control of arabidopsis seedling chlorophyll biosynthesis," *Frontiers in Plant Science*, vol. 8, 2017.

[2] J. Putterill, R. Laurie, and R. Macknight, "It's time to flower: the genetic control of flowering time," *BioEssays*, vol. 26, no. 4, pp. 363–373, 2004.

[3] A. L. Norris and T. H. Kunz, "Effects of solar radiation on animal thermoregulation," *Solar radiation*, pp. 195–220, 2012.

[4] F. Anwar, F. N. Chaudhry, S. Nazeer, N. Zaman, and S. Azam, "Causes of ozone layer depletion and its effects on human," *Atmospheric and Climate Sciences*, vol. 6, no. 1, pp. 129–134, 2015.

[5] C. Kielbassa, L. Roza, and B. Epe, "Wavelength dependence of oxidative dna damage induced by uv and visible light.," *Carcinogenesis*, vol. 18, no. 4, pp. 811–816, 1997.

[6] D. I. Pattison, A. S. Rahmanto, and M. J. Davies, "Photo-oxidation of proteins," *Photochemical & Photobiological Sciences*, vol. 11, no. 1, pp. 38–53, 2012.

[7] R. P. Sinha and D.-P. Häder, "Uv-induced dna damage and repair: a review," *Photochemical & Photobiological Sciences*, vol. 1, no. 4, pp. 225–236, 2002.

[8] T. Carell and R. Epple, "Repair of uv light induced dna lesions: a comparative study with model compounds," *European journal of organic chemistry*, vol. 1998, no. 7, pp. 1245–1258, 1998.

[9] G. Prakash and D. E. Falvey, "Model studies of the (6-4) photoproduct dna photolyase: Synthesis and photosensitized splitting of a thymine-5, 6-oxetane," *Journal Of The American Chemical Society*, vol. 117, no. 45, pp. 11375–11376, 1995.

[10] T. Douki and J. Cadet, "Individual determination of the yield of the main uv-induced dimeric pyrimidine photoproducts in dna suggests a high mutagenicity of cc photolesions," *Biochemistry*, vol. 40, no. 8, pp. 2495–2501, 2001.

[11] J.-K. Kim, D. Patel, and B.-S. Choi, "Contrasting structural impacts induced by cis-syn cyclobutane dimer and (6–4) adduct in dna duplex decamers: implication in mutagenesis and repair activity," *Photochemistry and photobiology*, vol. 62, no. 1, pp. 44–50, 1995.

[12] C. J. Rudolph, A. L. Upton, and R. G. Lloyd, "Replication fork stalling and cell cycle arrest in uv-irradiated escherichia coli," *Genes & development*, vol. 21, no. 6, pp. 668–681, 2007.

[13] D. L. Mitchell, J. E. Vaughan, and R. S. Nairn, "Inhibition of transient gene expression in chinese hamster ovary cells by cyclobutane dimers and (6-4) photoproducts in transfected ultraviolet-irradiated plasmid dna," *Plasmid*, vol. 21, no. 1, pp. 21–30, 1989.

[14] H. Yokoyama and R. Mizutani, "Structural biology of dna (6-4) photoproducts formed by ultraviolet radiation and interactions with their binding proteins," *International journal of molecular sciences*, vol. 15, no. 11, pp. 20321–20338, 2014.

[15] D. L. Jones and B. K. Baxter, "Dna repair and photoprotection: Mechanisms of overcoming environmental ultraviolet radiation exposure in halophilic archaea," *Frontiers in microbiology*, vol. 8, p. 1882, 2017.

[16] A. Sancar, "Mechanisms of dna repair by photolyase and excision nuclease (nobel lecture)," *Angewandte Chemie International Edition*, vol. 55, no. 30, pp. 8502–8527, 2016.

[17] G.-M. Li, "Mechanisms and functions of dna mismatch repair," *Cell research*, vol. 18, no. 1, pp. 85–98, 2008.

[18] Z. Ozer, J. T. Reardon, D. S. Hsu, K. Malhotra, and A. Sancar, "The other function of dna photolyase: stimulation of excision repair of chemical damage to dna," *Biochemistry*, vol. 34, no. 49, pp. 15886–15889, 1995.

[19] M. E. Fox, B. J. Feldman, and G. Chu, "A novel role for dna photolyase: binding to dna damaged by drugs is associated with enhanced cytotoxicity in saccharomyces cerevisiae," *Molecular and Cellular Biology*, vol. 14, no. 12, pp. 8071–8077, 1994.

[20] R. P. Rastogi, A. Kumar, M. B. Tyagi, R. P. Sinha, *et al.*, "Molecular mechanisms of ultraviolet radiation-induced dna damage and repair," *Journal of nucleic acids*, vol. 2010, 2010.

[21] A. Vaisman and R. Woodgate, "Translesion dna polymerases in eukaryotes: what makes them tick?," *Critical reviews in biochemistry and molecular biology*, vol. 52, no. 3, pp. 274–303, 2017.

[22] C. Masutani, R. Kusumoto, S. Iwai, and F. Hanaoka, "Mechanisms of accurate translesion synthesis by human dna polymerase $\eta$," *The EMBO journal*, vol. 19, no. 12, pp. 3100–3109, 2000.

[23] R. E. Johnson, L. Haracska, S. Prakash, and L. Prakash, "Role of dna polymerase $\eta$ in the bypass of a (6-4) tt photoproduct," *Molecular and cellular biology*, vol. 21, no. 10, pp. 3558–3563, 2001.

[24] J. Wang, X. Du, W. Pan, X. Wang, and W. Wu, "Photoactivation of the cryptochrome/photolyase superfamily," *Journal of Photochemistry and Photobiology C: Photochemistry Reviews*, vol. 22, pp. 84–102, 2015.

[25] L. Essen and T. Klar, "Light-driven dna repair by photolyases," *Cellular and Molecular Life Sciences CMLS*, vol. 63, no. 11, pp. 1266–1277, 2006.

[26] A. Sancar, "Structure and function of dna photolyase and cryptochrome blue-light photoreceptors," *Chemical reviews*, vol. 103, no. 6, pp. 2203–2238, 2003.

[27] D. J. Walter, M. Boswell, S. M. V. de García, S. M. Walter, E. W. Breitenfeldt, W. Boswell, and R. B. Walter, "Characterization and differential expression of cpd and 6–4 dna photolyases in xiphophorus species and interspecies hybrids," *Comparative Biochemistry and Physiology Part C: Toxicology & Pharmacology*, vol. 163, pp. 77–85, 2014.

[28] A. Sancar, "Structure and function of dna photolyase," *Biochemistry*, vol. 33, no. 1, pp. 2–9, 1994.

[29] B. D. Zoltowski, Y. Chelliah, A. Wickramaratne, L. Jarocha, N. Karki, W. Xu, H. Mouritsen, P. J. Hore, R. E. Hibbs, C. B. Green, *et al.*, "Chemical and structural analysis of a photoactive vertebrate cryptochrome from pigeon," *Proceedings of the National Academy of Sciences*, vol. 116, no. 39, pp. 19449–19457, 2019.

[30] C. Lin and D. Shalitin, "Cryptochrome structure and signal transduction," *Annual review of plant biology*, vol. 54, no. 1, pp. 469–496, 2003.

[31] K. Hitomi, K. Okamoto, H. Daiyasu, H. Miyashita, S. Iwai, H. Toh, M. Ishiura, and T. Todo, "Bacterial cryptochrome and photolyase: characterization of two photolyase-like genes of synechocystis sp. pcc6803," *Nucleic acids research*, vol. 28, no. 12, pp. 2353–2362, 2000.

[32] C. P. Selby and A. Sancar, "A cryptochrome/photolyase class of enzymes with single-stranded dna-specific photolyase activity," *Proceedings of the National Academy of Sciences*, vol. 103, no. 47, pp. 17696–17700, 2006.

[33] R. Pokorny, T. Klar, U. Hennecke, T. Carell, A. Batschauer, and L.-O. Essen, "Recognition and repair of uv lesions in loop structures of duplex dna by dash-type cryptochrome," *Proceedings of the National Academy of Sciences*, vol. 105, no. 52, pp. 21023–21027, 2008.

[34] S. Kiontke, T. Göbel, A. Brych, and A. Batschauer, "Dash-type cryptochromes–solved and open questions," *Biological Chemistry*, vol. 401, no. 12, pp. 1487–1493, 2020.

[35] X. Zhang, Z. Zheng, Y. He, L. Liu, C. Qu, and J. Miao, "Molecular cloning and expression of a cryptochrome gene cicry-dash1 from the antarctic microalga chlamydomonas sp. ice-l," *Molecular Biotechnology*, vol. 62, no. 2, pp. 91–103, 2020.

[36] S. Franz, E. Ignatz, S. Wenzel, H. Zielosko, E. P. G. N. Putu, M. Maestre-Reyna, M.-D. Tsai, J. Yamamoto, M. Mittag, and L.-O. Essen, "Structure of the bifunctional cryptochrome acry from chlamydomonas reinhardtii," *Nucleic acids research*, vol. 46, no. 15, pp. 8010–8022, 2018.

[37] J. J. Marizcurrena, S. Acosta, L. Canclini, P. Hernández, D. Vallés, T. Lamparter, and S. Castro-Sowinski, "A natural occurring bifunctional cpd/(6-4)-photolyase from the antarctic bacterium sphingomonas sp. uv9," *Applied Microbiology and Biotechnology*, vol. 104, no. 16, pp. 7037–7050, 2020.

[38] I. H. Kavakli, I. Baris, M. Tardu, Ş. Gül, H. Öner, S. Cal, S. Bulut, D. Yarparvar, Ç. Berkel, P. Ustaoğlu, *et al.*, "The photolyase/cryptochrome family of proteins as dna repair enzymes and transcriptional repressors," *Photochemistry and photobiology*, vol. 93, no. 1, pp. 93–103, 2017.

[39] G. C. G. Parico and C. L. Partch, "The tail of cryptochromes: an intrinsically disordered cog within the mammalian circadian clock," *Cell Communication and Signaling*, vol. 18, no. 1, pp. 1–9, 2020.

[40] H.-W. Park, S.-T. Kim, A. Sancar, and J. Deisenhofer, "Crystal structure of dna photolyase from escherichia coli," *Science*, vol. 268, no. 5219, pp. 1866–1872, 1995.

[41] K. Hitomi, L. DiTacchio, A. S. Arvai, J. Yamamoto, S.-T. Kim, T. Todo, J. A. Tainer, S. Iwai, S. Panda, and E. D. Getzoff, "Functional motifs in the (6-4) photolyase crystal structure make a comparative framework for dna repair photolyases and clock cryptochromes," *Proceedings of the National Academy of Sciences*, vol. 106, no. 17, pp. 6962–6967, 2009.

[42] B. D. Zoltowski, A. T. Vaidya, D. Top, J. Widom, M. W. Young, and B. R. Crane, "Structure of full-length drosophila cryptochrome," *Nature*, vol. 480, no. 7377, pp. 396–399, 2011.

[43] Z. Liu, X. Guo, C. Tan, J. Li, Y.-T. Kao, L. Wang, A. Sancar, and D. Zhong, "Electron tunneling pathways and role of adenine in repair of cyclobutane pyrimidine dimer by dna photolyase," *Journal of the American Chemical Society*, vol. 134, no. 19, pp. 8104–8114, 2012.

[44] K. Hitomi, H. Nakamura, S.-T. Kim, T. Mizukoshi, T. Ishikawa, S. Iwai, and T. Todo, "Role of two histidines in the (6-4) photolyase reaction," *Journal of Biological Chemistry*, vol. 276, no. 13, pp. 10103–10109, 2001.

[45] S. Weber, "Light-driven enzymatic catalysis of dna repair: a review of recent biophysical studies on photolyase," *Biochimica et Biophysica Acta (BBA)-Bioenergetics*, vol. 1707, no. 1, pp. 1–23, 2005.

[46] M. Maestre-Reyna, C.-H. Yang, E. Nango, W.-C. Huang, E. P. G. Ngurah Putu, W.-J. Wu, P.-H. Wang, S. Franz-Badur, M. Saft, H.-J. Emmerich, *et al.*, "Serial crystallography captures dynamic control of sequential electron and proton transfer events in a flavoenzyme," *Nature Chemistry*, pp. 1–9, 2022.

[47] J. L. Johnson, S. Hamm-Alvarez, G. Payne, G. B. Sancar, K. Rajagopalan, and A. Sancar, "Identification of the second chromophore of escherichia coli and yeast dna photolyases as 5, 10-methenyltetrahydrofolate.," *Proceedings of the National Academy of Sciences*, vol. 85, no. 7, pp. 2046–2050, 1988.

[48] P. Scheerer, F. Zhang, J. Kalms, D. von Stetten, N. Krauß, I. Oberpichler, and T. Lamparter, "The class iii cyclobutane pyrimidine dimer photolyase structure reveals a new antenna chromophore binding site and alternative photoreduction pathways," *Journal of Biological Chemistry*, vol. 290, no. 18, pp. 11504–11514, 2015.

[49] M. Fujihashi, N. Numoto, Y. Kobayashi, A. Mizushima, M. Tsujimura, A. Nakamura, Y. Kawarabayasi, and K. Miki, "Crystal structure of archaeal photolyase from sulfolobus tokodaii with two fad molecules: implication of a novel light-harvesting cofactor," *Journal of molecular biology*, vol. 365, no. 4, pp. 903–910, 2007.

[50] T. Tamada, K. Kitadokoro, Y. Higuchi, K. Inaka, A. Yasui, P. E. de Ruiter, A. Eker, and K. Miki, "Crystal structure of dna photolyase from anacystis nidulans.," *Nature structural biology*, vol. 4, no. 11, pp. 887–891, 1997.

[51] S. Kiontke, P. Gnau, R. Haselsberger, A. Batschauer, and L.-O. Essen, "Structural and evolutionary aspects of antenna chromophore usage by class ii photolyases," *Journal of Biological Chemistry*, vol. 289, no. 28, pp. 19659–19669, 2014.

[52] A. F. Glas, M. J. Maul, M. Cryle, T. R. Barends, S. Schneider, E. Kaya, I. Schlichting, and T. Carell, "The archaeal cofactor f0 is a light-harvesting antenna chromophore in eukaryotes," *Proceedings of the National Academy of Sciences*, vol. 106, no. 28, pp. 11540–11545, 2009.

[53] S. Chen, C. Liu, C. Zhou, Z. Wei, Y. Li, L. Xiong, L. Yan, J. Lv, L. Shen, and L. Xu, "Identification and characterization of a prokaryotic 6-4 photolyase from synechococcus elongatus with a deazariboflavin antenna chromophore," *Nucleic Acids Research*, vol. 50, no. 10, pp. 5757–5771, 2022.

[54] T. Klar, G. Kaiser, U. Hennecke, T. Carell, A. Batschauer, and L.-O. Essen, "Natural and non-natural antenna chromophores in the dna photolyase from thermus thermophilus," *ChemBioChem*, vol. 7, no. 11, pp. 1798–1806, 2006.

[55] A. von Zadow, E. Ignatz, R. Pokorny, L.-O. Essen, and G. Klug, "Rhodobacter sphaeroides cryb is a bacterial cryptochrome with (6–4) photolyase activity," *The FEBS journal*, vol. 283, no. 23, pp. 4291–4309, 2016.

[56] I. Chaves, R. Pokorny, M. Byrdin, N. Hoang, T. Ritz, K. Brettel, L.-O. Essen, G. T. van der Horst, A. Batschauer, M. Ahmad, *et al.*, "The cryptochromes: blue light photoreceptors in plants and animals," *Annual review of plant biology*, vol. 62, no. 1, pp. 335–364, 2011.

[57] A. T. Vaidya, D. Top, C. C. Manahan, J. M. Tokuda, S. Zhang, L. Pollack, M. W. Young, and B. R. Crane, "Flavin reduction activates drosophila cryptochrome," *Proceedings of the National Academy of Sciences*, vol. 110, no. 51, pp. 20455–20460, 2013.

[58] P. Müller, J. Yamamoto, R. Martin, S. Iwai, and K. Brettel, "Discovery and functional analysis of a 4th electron-transferring tryptophan conserved exclusively in animal cryptochromes and (6-4) photolyases," *Chemical Communications*, vol. 51, no. 85, pp. 15502–15505, 2015.

[59] D. Nohr, S. Franz, R. Rodriguez, B. Paulus, L.-O. Essen, S. Weber, and E. Schleicher, "Extended electron-transfer in animal cryptochromes mediated by a tetrad of aromatic amino acids," *Biophysical journal*, vol. 111, no. 2, pp. 301–311, 2016.

[60] S. Kiontke, Y. Geisselbrecht, R. Pokorny, T. Carell, A. Batschauer, and L.-O. Essen, "Crystal structures of an archaeal class ii dna photolyase and its complex with uv-damaged duplex dna," *The EMBO journal*, vol. 30, no. 21, pp. 4437–4449, 2011.

[61] T. Biskup, K. Hitomi, E. D. Getzoff, S. Krapf, T. Koslowski, E. Schleicher, and S. Weber, "Unexpected electron transfer in cryptochrome identified by time-resolved epr spectroscopy," *Angewandte Chemie International Edition*, vol. 50, no. 52, pp. 12647–12651, 2011.

[62] P. Müller, J.-P. Bouly, K. Hitomi, V. Balland, E. D. Getzoff, T. Ritz, and K. Brettel, "Atp binding turns plant cryptochrome into an efficient natural photoswitch," *Scientific Reports*, vol. 4, no. 1, pp. 1–11, 2014.

[63] D. Holub, H. Ma, N. Krauß, T. Lamparter, M. Elstner, and N. Gillet, "Functional role of an unusual tyrosine residue in the electron transfer chain of a prokaryotic (6–4) photolyase," *Chemical science*, vol. 9, no. 5, pp. 1259–1272, 2018.

[64] P. Müller, E. Ignatz, S. Kiontke, K. Brettel, and L.-O. Essen, "Sub-nanosecond tryptophan radical deprotonation mediated by a protein-bound water cluster in class ii dna photolyases," *Chemical science*, vol. 9, no. 5, pp. 1200–1212, 2018.

[65] Z. Liu, C. Tan, X. Guo, J. Li, L. Wang, A. Sancar, and D. Zhong, "Determining complete electron flow in the cofactor photoreduction of oxidized photolyase," *Proceedings of the National Academy of Sciences*, vol. 110, no. 32, pp. 12966–12971, 2013.

[66] C. Aubert, M. H. Vos, P. Mathis, A. P. Eker, and K. Brettel, "Intraprotein radical transfer during photoactivation of dna photolyase," *Nature*, vol. 405, no. 6786, pp. 586–590, 2000.

[67] A. Lukacs, A. P. Eker, M. Byrdin, K. Brettel, and M. H. Vos, "Electron hopping through the 15 å triple tryptophan molecular wire in dna photolyase occurs within 30 ps," *Journal of the American Chemical Society*, vol. 130, no. 44, pp. 14394–14395, 2008.

[68] I. M. M. Wijaya, T. Domratcheva, T. Iwata, E. D. Getzoff, and H. Kandori, "Single hydrogen bond donation from flavin n5 to proximal asparagine ensures fad reduction in dna photolyase," *Journal of the American Chemical Society*, vol. 138, no. 13, pp. 4368–4376, 2016.

[69] M. J. Damiani, J. J. Nostedt, and M. A. O'Neill, "Impact of the n5-proximal asn on the thermodynamic and kinetic stability of the semiquinone radical in photolyase," *Journal of Biological Chemistry*, vol. 286, no. 6, pp. 4382–4391, 2011.

[70] A. Berndt, T. Kottke, H. Breitkreuz, R. Dvorsky, S. Hennig, M. Alexander, and E. Wolf, "A novel photoreaction mechanism for the circadian blue light photoreceptor drosophila cryptochrome," *Journal of Biological Chemistry*, vol. 282, no. 17, pp. 13011–13021, 2007.

[71] J. Yamamoto, P. Plaza, and K. Brettel, "Repair of (6-4) lesions in dna by (6-4) photolyase: 20 years of quest for the photoreaction mechanism," *Photochemistry and photobiology*, vol. 93, no. 1, pp. 51–66, 2017.

[72] Z. Liu, C. Tan, X. Guo, Y.-T. Kao, J. Li, L. Wang, A. Sancar, and D. Zhong, "Dynamics and mechanism of cyclobutane pyrimidine dimer repair by dna photolyase," *Proceedings of the National Academy of Sciences*, vol. 108, no. 36, pp. 14831–14836, 2011.

[73] Y.-T. Kao, C. Saxena, L. Wang, A. Sancar, and D. Zhong, "Femtochemistry in enzyme catalysis: Dna photolyase," *Cell biochemistry and biophysics*, vol. 48, no. 1, pp. 32–44, 2007.

[74] K. Brettel, P. Muller, and J. Yamamoto, "Kinetics of electron returns in successive two-photon dna repair by (6-4) photolyase," *ACS Catalysis*, vol. 12, no. 5, pp. 3041–3045, 2022.

[75] M. J. Maul, T. R. Barends, A. F. Glas, M. J. Cryle, T. Domratcheva, S. Schneider, I. Schlichting, and T. Carell, "Crystal structure and mechanism of a dna (6-4) photolyase," *Angewandte Chemie International Edition*, vol. 47, no. 52, pp. 10076–10080, 2008.

[76] G. Rhodes, *Crystallography made crystal clear: a guide for users of macromolecular models*. Elsevier, 2010.

[77] B. Rupp, *Biomolecular crystallography: principles, practice, and application to structural biology*. Garland Science, 2009.

[78] A. McPherson, "Introduction to protein crystallization," *Methods*, vol. 34, no. 3, pp. 254–265, 2004.

[79] N. E. Chayen and E. Saridakis, "Protein crystallization: from purified protein to diffraction-quality crystal," *Nature methods*, vol. 5, no. 2, pp. 147–153, 2008.

[80] W. Liu, D. Wacker, C. Gati, G. W. Han, D. James, D. Wang, G. Nelson, U. Weierstall, V. Katritch, A. Barty, *et al.*, "Serial femtosecond crystallography of g protein–coupled receptors," *Science*, vol. 342, no. 6165, pp. 1521–1524, 2013.

[81] A. Shilova, H. Lebrette, O. Aurelius, J. Nan, M. Welin, R. Kovacic, S. Ghosh, C. Safari, R. J. Friel, M. Milas, *et al.*, "Current status and future opportunities for serial crystallography at max iv laboratory," *Journal of Synchrotron Radiation*, vol. 27, no. 5, pp. 1095–1102, 2020.

[82] A. Chernov, "Estimates of internal stress and related mosaicity in solution grown crystals: proteins," *Journal of crystal growth*, vol. 196, no. 2-4, pp. 524–534, 1999.

[83] P. Edlund, H. Takala, E. Claesson, L. Henry, R. Dods, H. Lehtivuori, M. Panman, K. Pande, T. White, T. Nakane, *et al.*, "The room temperature crystal structure of a bacterial phytochrome determined by serial femtosecond crystallography," *Scientific reports*, vol. 6, no. 1, pp. 1–9, 2016.

[84] R. Dods, P. Båth, D. Arnlund, K. R. Beyerlein, G. Nelson, M. Liang, R. Harimoorthy, P. Berntsen, E. Malmerberg, L. Johansson, *et al.*, "From macrocrystals to microcrystals: a strategy for membrane protein serial crystallography," *Structure*, vol. 25, no. 9, pp. 1461–1468, 2017.

[85] E. Claesson, W. Y. Wahlgren, H. Takala, S. Pandey, L. Castillon, V. Kuznetsova, L. Henry, M. Panman, M. Carrillo, J. Kübel, *et al.*, "The primary structural photoresponse of phytochrome proteins captured by a femtosecond x-ray laser," *Elife*, vol. 9, p. e53514, 2020.

[86] C. Kupitz, I. Grotjohann, C. E. Conrad, S. Roy-Chowdhury, R. Fromme, and P. Fromme, "Microcrystallization techniques for serial femtosecond crystallography using photosystem ii from thermosynechococcus elongatus as a model system," *Philosophical Transactions of the Royal Society B: Biological Sciences*, vol. 369, no. 1647, p. 20130316, 2014.

[87] P. Evans and A. McCoy, "An introduction to molecular replacement," *Acta Crystallographica Section D: Biological Crystallography*, vol. 64, no. 1, pp. 1–10, 2008.

[88] A. J. McCoy, R. W. Grosse-Kunstleve, P. D. Adams, M. D. Winn, L. C. Storoni, and R. J. Read, "Phaser crystallographic software," *Journal of applied crystallography*, vol. 40, no. 4, pp. 658–674, 2007.

[89] R. J. Read, "Pushing the boundaries of molecular replacement with maximum likelihood," *Acta Crystallographica Section D: Biological Crystallography*, vol. 57, no. 10, pp. 1373–1382, 2001.

[90] K. Rajashankar and Z. Dauter, "Data collection for crystallographic structure determination," in *Structural Genomics and Drug Discovery*, pp. 211–237, Springer, 2014.

[91] P. Emsley and K. Cowtan, "Coot: model-building tools for molecular graphics," *Acta crystallographica section D: biological crystallography*, vol. 60, no. 12, pp. 2126–2132, 2004.

[92] E. F. Garman, "Radiation damage in macromolecular crystallography: what is it and why should we care?," *Acta Crystallographica Section D: Biological Crystallography*, vol. 66, no. 4, pp. 339–351, 2010.

[93] V. Pfanzagl, J. H. Beale, H. Michlits, D. Schmidt, T. Gabler, C. Obinger, K. Djinović-Carugo, and S. Hofbauer, "X-ray–induced photoreduction of heme metal centers rapidly induces active-site perturbations in a protein-independent manner," *Journal of Biological Chemistry*, vol. 295, no. 39, pp. 13488–13501, 2020.

[94] J. M. Holton, "A beginner's guide to radiation damage," *Journal of synchrotron radiation*, vol. 16, no. 2, pp. 133–142, 2009.

[95] K. S. Paithankar and E. F. Garman, "Know your dose: Raddose," *Acta Crystallographica Section D: Biological Crystallography*, vol. 66, no. 4, pp. 381–388, 2010.

[96] H. R. Powell, "X-ray data processing," *Bioscience reports*, vol. 37, no. 5, 2017.

[97] P. A. Karplus and K. Diederichs, "Assessing and maximizing data quality in macromolecular crystallography," *Current opinion in structural biology*, vol. 34, pp. 60–68, 2015.

[98] P. A. Karplus and K. Diederichs, "Linking crystallographic model and data quality," *Science*, vol. 336, no. 6084, pp. 1030–1033, 2012.

[99] H. N. Chapman, C. Caleman, and N. Timneanu, "Diffraction before destruction," *Philosophical Transactions of the Royal Society B: Biological Sciences*, vol. 369, no. 1647, p. 20130313, 2014.

[100] A. R. Pearson and P. Mehrabi, "Serial synchrotron crystallography for time-resolved structural biology," *Current Opinion in Structural Biology*, vol. 65, pp. 168–174, 2020.

[101] S.-Y. Park, H. Choi, C. Eo, Y. Cho, and K. H. Nam, "Fixed-target serial synchrotron crystallography using nylon mesh and enclosed film-based sample holder," *Crystals*, vol. 10, no. 9, p. 803, 2020.

[102] C. Mueller, A. Marx, S. W. Epp, Y. Zhong, A. Kuo, A. Balo, J. Soman, F. Schotte, H. Lemke, R. Owen, *et al.*, "Fixed target matrix for femtosecond time-resolved and in situ serial micro-crystallography," *Structural Dynamics*, vol. 2, no. 5, p. 054302, 2015.

[103] L. C. Johansson, B. Stauch, A. Ishchenko, and V. Cherezov, "A bright future for serial femtosecond crystallography with xfels," *Trends in biochemical sciences*, vol. 42, no. 9, pp. 749–762, 2017.

[104] U. Weierstall, D. James, C. Wang, T. A. White, D. Wang, W. Liu, J. C. Spence, R. Bruce Doak, G. Nelson, P. Fromme, *et al.*, "Lipidic cubic phase injector facilitates membrane protein serial femtosecond crystallography," *Nature communications*, vol. 5, no. 1, pp. 1–6, 2014.

[105] M. Sugahara, E. Mizohata, E. Nango, M. Suzuki, T. Tanaka, T. Masuda, R. Tanaka, T. Shimamura, Y. Tanaka, C. Suno, *et al.*, "Grease matrix as a versatile carrier of proteins for serial crystallography," *Nature methods*, vol. 12, no. 1, pp. 61–63, 2015.

[106] M. Sugahara, T. Nakane, T. Masuda, M. Suzuki, S. Inoue, C. Song, R. Tanaka, T. Nakatsu, E. Mizohata, F. Yumoto, *et al.*, "Hydroxyethyl cellulose matrix applied to serial crystallography," *Scientific reports*, vol. 7, no. 1, pp. 1–9, 2017.

[107] M. Sugahara, C. Song, M. Suzuki, T. Masuda, S. Inoue, T. Nakane, F. Yumoto, E. Nango, R. Tanaka, K. Tono, *et al.*, "Oil-free hyaluronic acid matrix for serial femtosecond crystallography," *Scientific reports*, vol. 6, no. 1, pp. 1–6, 2016.

[108] C. E. Conrad, S. Basu, D. James, D. Wang, A. Schaffer, S. Roy-Chowdhury, N. A. Zatsepin, A. Aquila, J. Coe, C. Gati, *et al.*, "A novel inert crystal delivery medium for serial femtosecond crystallography," *IUCrJ*, vol. 2, no. 4, pp. 421–430, 2015.

[109] R. Fromme, A. Ishchenko, M. Metz, S. R. Chowdhury, S. Basu, S. Boutet, P. Fromme, T. A. White, A. Barty, J. C. Spence, *et al.*, "Serial femtosecond crystallography of soluble proteins in lipidic cubic phase," *IUCrJ*, vol. 2, no. 5, pp. 545–551, 2015.

[110] A. Barty, R. A. Kirian, F. R. Maia, M. Hantke, C. H. Yoon, T. A. White, and H. Chapman, "Cheetah: software for high-throughput reduction and analysis of serial femtosecond x-ray diffraction data," *Journal of applied crystallography*, vol. 47, no. 3, pp. 1118–1131, 2014.

[111] T. A. White, R. A. Kirian, A. V. Martin, A. Aquila, K. Nass, A. Barty, and H. N. Chapman, "Crystfel: a software suite for snapshot serial crystallography," *Journal of applied crystallography*, vol. 45, no. 2, pp. 335–341, 2012.

[112] W. Kabsch, "xds," *Acta Crystallographica Section D: Biological Crystallography*, vol. 66, no. 2, pp. 125–132, 2010.

[113] T. G. G. Battye, L. Kontogiannis, O. Johnson, H. R. Powell, and A. G. Leslie, "imosflm: a new graphical interface for diffraction-image processing with mosflm," *Acta Crystallographica Section D: Biological Crystallography*, vol. 67, no. 4, pp. 271–281, 2011.

[114] A. J. M. Duisenberg, "Indexing in single-crystal diffractometry with an obstinate list of reflections," *Journal of applied crystallography*, vol. 25, no. 2, pp. 92–96, 1992.

[115] T. A. White, "Processing serial crystallography data with crystfel: a step-by-step guide," *Acta Crystallographica Section D*, vol. 75, no. 2, pp. 219–233, 2019.

[116] H. Liu and J. C. Spence, "Xfel data analysis for structural biology," *Quantitative Biology*, vol. 4, no. 3, pp. 159–176, 2016.

[117] I. G. Shabalin, P. J. Porebski, and W. Minor, "Refining the macromolecular model–achieving the best agreement with the data from x-ray diffraction experiment," *Crystallography reviews*, vol. 24, no. 4, pp. 236–262, 2018.

[118] T. Ursby and D. Bourgeois, "Improved estimation of structure-factor difference amplitudesfrom poorly accurate data," *Acta Crystallographica Section A: Foundations of Crystallography*, vol. 53, no. 5, pp. 564–575, 1997.

[119] Z. Ren, B. Perman, V. Šrajer, T.-Y. Teng, C. Pradervand, D. Bourgeois, F. Schotte, T. Ursby, R. Kort, M. Wulff, *et al.*, "A molecular movie at 1.8 å resolution displays the photocycle of photoactive yellow protein, a eubacterial blue-light receptor, from nanoseconds to seconds," *Biochemistry*, vol. 40, no. 46, pp. 13788–13801, 2001.

[120] C. Wickstrand, G. Katona, T. Nakane, P. Nogly, J. Standfuss, E. Nango, and R. Neutze, "A tool for visualizing protein motions in time-resolved crystallography," *Structural Dynamics*, vol. 7, no. 2, p. 024701, 2020.

[121] P. Nogly, T. Weinert, D. James, S. Carbajo, D. Ozerov, A. Furrer, D. Gashi, V. Borin, P. Skopintsev, K. Jaeger, K. Nass, P. Båth, R. Bosman, J. Koglin, M. Seaberg, T. Lane, D. Kekilli, S. Brünle, T. Tanaka, W. Wu, C. Milne, T. White, A. Barty, U. Weierstall, V. Panneels, E. Nango, S. Iwata, M. Hunter, I. Schapiro, G. Schertler, R. Neutze, and S. Jörg, "Retinal isomerization in bacteriorhodopsin captured by a femtosecond x-ray laser," *Science*, vol. 361, no. 6398, p. eaat0094, 2018.

[122] K. Pande, C. D. Hutchison, G. Groenhof, A. Aquila, J. S. Robinson, J. Tenboer, S. Basu, S. Boutet, D. P. DePonte, M. Liang, *et al.*, "Femtosecond structural dynamics drives the trans/cis isomerization in photoactive yellow protein," *Science*, vol. 352, no. 6286, pp. 725–729, 2016.

[123] P. Skopintsev, D. Ehrenberg, T. Weinert, D. James, R. K. Kar, P. J. Johnson, D. Ozerov, A. Furrer, I. Martiel, F. Dworkowski, *et al.*, "Femtosecond-to-millisecond structural changes in a light-driven sodium pump," *Nature*, vol. 583, no. 7815, pp. 314–318, 2020.

[124] N. Ramírez, M. Serey, A. Illanes, M. Piumetti, and C. Ottone, "Immobilization strategies of photolyases: Challenges and perspectives for dna repairing application," *Journal of Photochemistry and Photobiology B: Biology*, vol. 215, p. 112113, 2021.

[125] C. Navarrete-Dechent and M. Molgó, "The use of a sunscreen containing dna-photolyase in the treatment of patients with field cancerization and multiple actinic keratoses: a case-series," *Dermatology Online Journal*, vol. 23, no. 1, 2017.